Check for updates

ADVANCED OPTICAL MATERIALS
www.advopticalmat.de

3D Radial Junctions for Robust and Flexible Optoelectronics

*Shaobo Zhang and Linwei Yu**

Marrying nanostructures with thin films is a recent trend in flexible optoelectronics to improve light trapping and mechanical stability. Radial junction (RJ) a-Si:H thin film optoelectronics, directly deposited upon the vapor-liquid-solid (VLS) grown silicon nanowires (SiNWs), can pave the way to achieving excellent flexibility and a high power-to-weight ratio (PTWR). Thanks to their vertical-standing geometry, SiNWs framework can enhance the mechanical stability of RJ units, by keeping the working region far away from the stress-rich substrate surface. Using low-melting-point metals as catalysts, the SiNW array can be fabricated at a low temperature down to 350 °C in a PECVD system, making it possible to directly construct robust RJ units on flexible, low-cost substrates, such as Al foil. In this review, the recent progress of the flexible RJ a-Si:H thin film solar cells/photodetectors that are directly fabricated on the surface of low-cost flexible substrates is reviewed. Moreover, these RJ flexible optoelectronics are demonstrated for use in wearable and real-time health monitoring, and as cardiac pacemakers for heart stimulation. This RJ technology highlights a promising potential to establish high-performance, low-cost, mechanically stable flexible optoelectronic for wearable, portable applications.

1. Introduction

Applying many flexible, portable, light-weight, and biomimetic/bio-friendly optoelectronic devices in diversified wearable scenarios has attracted much attention, for their capacity of comfortably and conformally fitting to human skin or organs, which is highly suitable for biomedical or clinical applications, as shown in **Figure 1**, such as electronic skin, bionic devices, physiological signal monitors or curing diseases.[1–8] Traditionally, the crystalline silicon (c-Si) material is the first candidate to fabricate high-quality photovoltaics,[9,10] but the c-Si wafer is rigid, bulky, and hard, making it face a dilemma when used for flexible applications. To afford such flexible application demand, a rather complicated and expensive fabrication process is needed, such as chemical etching or exfoliation to prepare ultra-thin monocrystalline silicon wafers (thickness <40 μm),[11–14] or using the top-down method to fabricate vertical micro/nanowire that then transferred onto/into organic substrate/encapsulation,[15–17] or designing serpentine/grid nanowire (by using high-accuracy photolithography or electron beam lithography),[18] or fabricating organic-inorganic hybrid devices, for example using poly (3,4-ethylenedioxythiophene):polystyrene sulfonate (PEDOT:PSS) as a p-type window.[19,20]

Therefore, the thin films prepared on flexible substrates can have reasonable mechanical properties, which may be a better/simpler choice for fabricating mechanically stable flexible photovoltaics/photodetectors.[5,8,26–28] Recently, organic materials have attracted much attention for their excellent bendable and stretchable characteristic, which have been widely applied in flexible, wearable devices, and lots of published works demonstrated successful experimental trials in labs.[7,29–33] Unfortunately, limited by their physical properties (such as instability in the air, low carrier mobility, and so on), using organic materials as the active layers to fabricate optoelectronic/electronic devices usually cannot obtain a competitive electrical performance.[34–40] Therefore, inorganic semiconductor thin films have attracted more attention for fabricating robust and stable devices. Hydrogenated amorphous silicon (a-Si:H) thin films can be prepared by using a low-cost, large-scale, and industrial-mature technique, which should be more proper for preparing flexible thin film optoelectronic devices. In contrast to perovskite,[41–48] cadmium telluride (CdTe),[49–53] and copper indium gallium selenium (CIGS),[54–60] III–V semiconductor [61–65] materials, a-Si:H thin films do not contain any toxic or heavy-metal elements or rare-earth elements.[59,66–69] However, the conventional planar thin films directly deposited on the surface of flexible substrates will face a rather serious challenge that the slight bending of substrates will leave large cracks, as shown in **Figure 2**, which would largely worsen the electrical performance and even result in a failure.[70–72] To address this dilemma, researchers tried to design the geometric architecture of optoelectronic devices to keep the deposited thin film far away from the substrate-bended stress, [71,73–75] for example fabricating a radial junction (RJ) structure.[76–79]

S. Zhang
College of Physical Science and Technology/Microelectronics Industry Research Institute
Yangzhou University
Yangzhou 225002, P.R. China

L. Yu
School of Electronics Science and Engineering/National Laboratory of Solid State Microstructures/Collaborative Innovation Center of Advanced Microstructures
Nanjing University
Nanjing 210093, P.R. China
E-mail: yulinwei@nju.edu.cn

The ORCID identification number(s) for the author(s) of this article can be found under https://doi.org/10.1002/adom.202302121

DOI: 10.1002/adom.202302121

 © 2024 Wiley-VCH GmbH

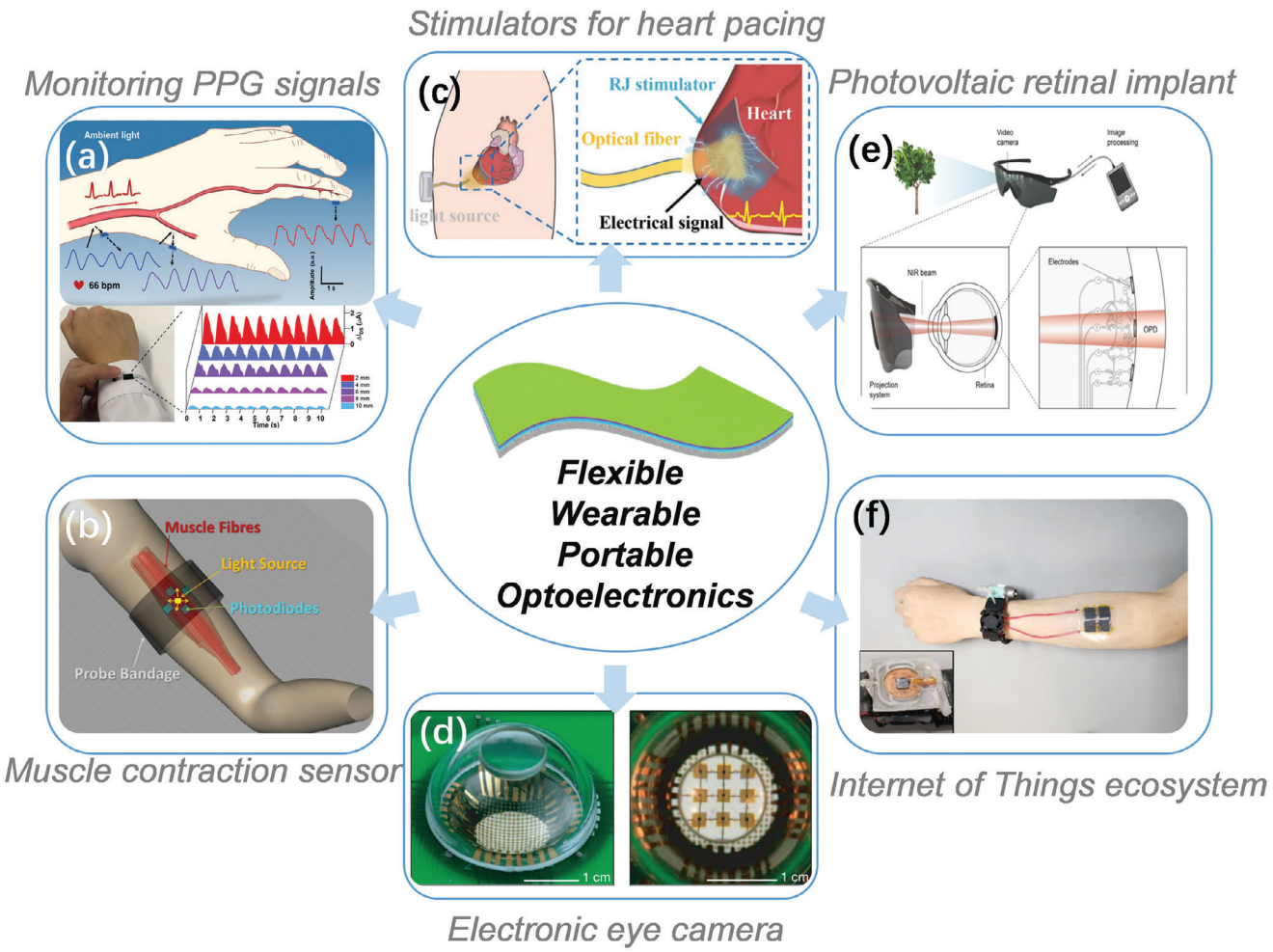


Figure 1. Bio-applications of the flexible optoelectronics. a) Illustration of perovskite solar cell-gated organic electrochemical transistors for flexible photodetectors to monitor photoplethysmogram signals from three different locations of the human body under ambient light.[21] Copyright 2023 Wiley-VCH GmbH, Weinheim. b) A sketch map of the muscle contraction sensor shows an arm containing muscle fibers, and the probe bandage consisting of a source and four photodiodes on top of the arm.[7] Copyright 2015 Wiley-VCH GmbH, Weinheim. c) Diagram of the RJ photovoltaic simulator for heart pacing under modulated 650 nm laser illumination.[22] Copyright 2020 Wiley-VCH GmbH, Weinheim. d) Left: photo of the camera after integration with a transparent hemispherical cap (compressible silicon optoelectronics); right: a close-up photo of the system as viewed directly through the imaging lens.[23] Copyright 2008 Nature. e) Concept of photovoltaic retinal implant based on NIR organic photodiodes.[24] Copyright 2018 Wiley-VCH GmbH, Weinheim. f) Photograph of the Internet of Things ecosystem based on flexible perovskite solar cells under ambient light. The inset shows the wearable haptic device.[25] Copyright 2023 Nature.

Radially stacked *p-n* or *p-i-n* junction designs have attracted much attention, where the charge collection path is in the radial direction and the light path is in the vertical direction along the core.[82–86] To form such core–shell RJ structure, different designed nano-architectures have been investigated/used as the core, such as nanowire,[86–89] nanorod,[90–93] nanopyramid,[94–96] nano-cone,[97–99] and so on. Among these nano-architectures, the nanowire is the most popular choice to fabricate such radially stacked core-shell structure, for example, using the Si nanowire (SiNW) as a core to host amorphous Si thin film to form c-Si/a-Si core–shell,[100–102] or III–V thin film as a shell to form such as Si/InP core–shell.[103,104] Besides, other kinds of nanowires have been used as the core to host subsequently deposited thin films such as ZnO nanowire,[105,106] which has been reported as the core to host a-Si:H *p-i-n* thin films to improve the mechanical flexibility.[107] In recent years, III–V semiconductor nanowires, which emerged as promising optoelectronics (for example, solar cells, photodetectors, and LEDs), have attracted much attention because of their direct and suitable bandgap, inherent high optical absorption, minimized light reflection, flexibility in device design, efficient charge collection in the radial direction.[63,108–113] There has been considerable research on III–V nanowire-based RJ devices, such as GaAs/AlGaAs core–shell,[61,62,114,115] InAs/InAlAs core–shell,[116–118] and so on. Such III–V nanowire-based RJ structures are potential candidates for fabricating flexible sensors to be incorporated in skin patches or integrated onto clothes.[119,120] However, marrying the SiNW framework to industrial-mature a-Si:H thin film may be a better choice for fabricating lightweight, and mechanically stable flexible optoelectronics, considering its excellent weak light

© 2024 Wiley-VCH GmbH

21951071, 2024, 9, Downloaded from https://advanced.onlinelibrary.wiley.com/doi/10.1002/adom.202302121 by Nanjing University, Wiley Online Library on [04/11/2026]. See the Terms and Conditions (https://onlinelibrary.wiley.com/terms-and-conditions) on Wiley Online Library for rules of use; OA articles are governed by the applicable Creative Commons License

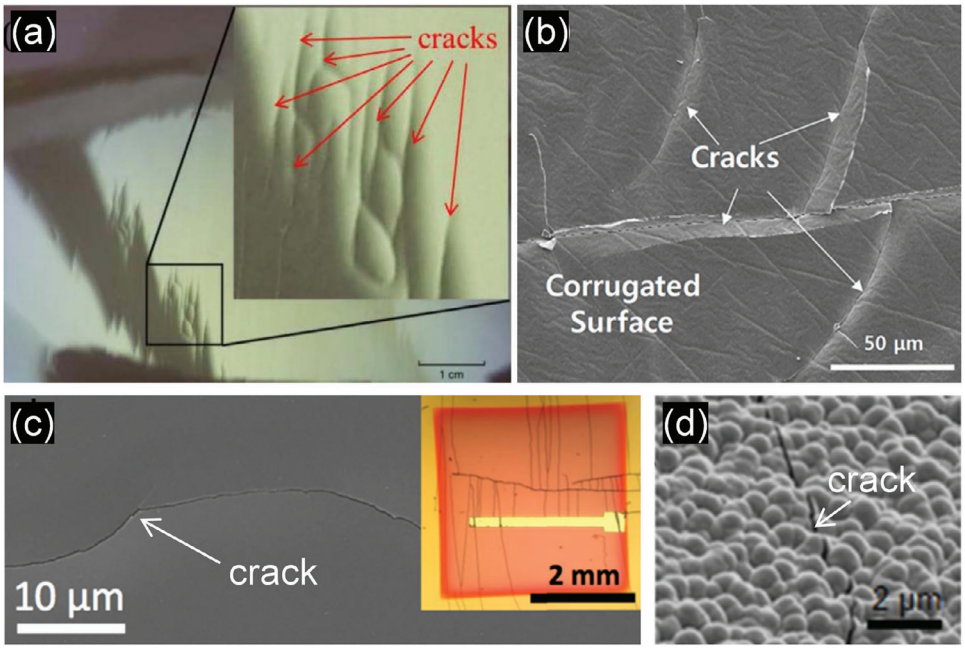


Figure 2. a) Photo of AZO thin film with cracks on bare PEN substrate.[70] Copyright 2018 Elsevier. b) SEM image of a-Si:H layer on PDMS substrate.[80] Copyright 2019 American Chemical Society. c) SEM image of planar a-Si:H devices based on spin-coated flat PI substrates (the inset is an optical photograph).[71] Copyright 2016 Elsevier. d) SEM image of crack propagation on the surface of flexible a-Si:H solar cells after bending.[81] Copyright 2015 Wiley-VCH GmbH, Weinheim.

response, low cost, abundant reserves, and simple fabrication process.[121–123]

Compared to conventional planar a-Si:H photovoltaics, constructing the 3D SiNW framework offers a strong light-trapping effect that can allow for the use of the absorber layer with a very thin thickness (<100 nm), helping to decouple the effective light absorption length and the carrier collection distance, thus an enhanced photo-generated carrier collection and better stability under sunlight exposure can be achieved in the RJ structured a-Si:H thin film photovoltaics.[124,125] Furthermore, the core SiNWs can serve as firmly anchored sites to host the deposited a-Si:H thin-film multilayers, protecting the sidewall working region away from the stress-rich flexible substrate surface and ensuring excellent mechanical flexibility.[77,126] Normally, the SiNW fabrication methods can be classified into two classes: top-down and bottom-up. The top-down methods usually depend on the etching process, and the bottom-up methods usually depend on the self-assembly process, such as the vapor–liquid–solid (VLS) process.[127] During a typical VLS growth, the metal catalyst, such as gold (Au), is heated to form catalyst droplets, which will absorb the decomposed gaseous silicon precursor, and establish three silicon atom states: i) supersaturation state in the metal catalyst, then ii) precipitation to form crystalline seeds, then iii) continuous precipitation at the bottom of the liquid–solid interface to form the SiNW.[125] However, this high-temperature process is incompatible with the most of market-available low-cost flexible substrates. Therefore, a low-temperature VLS growth process in the plasma-enhanced chemical vapor deposition (PECVD) system would be a better choice for constructing the SiNWs framework, allowing the use of very low-cost and flexible substrates. Thus, it is possible to fabricate highly flexible and robust a-Si:H RJ thin film optoelectronic devices around the VLS-grown SiNWs, which can be directly prepared upon very cheap and ultrasoft Al foil substrates, to achieve a very high power-to-weight ratio (PTWR).[77,78]

This paper aims to review recent progress in the flexible RJ a-Si:H thin film solar cells/photodetectors and their bio-applications. In Section 2, the VLS growth catalyzed by the low-melting-point (LMP) metal catalyst in a PECVD system and device fabrication are introduced. In Section 3, the optoelectronic properties of RJ units are introduced. Finally, the flexible RJ optoelectronics and some bio-applications are presented in Section 4, followed by a summary.

2. Material Growth and Device Fabrication

2.1. LMP Metal Catalyst Choice

As known, the VLS mechanism, catalyzed by metal catalyst droplets using a conventional CVD system, was first raised by R.S. Wagner and W.C. Ellis,[127] which is fundamental for the growth of crystal SiNWs, as shown in **Figure 3**a,b. During this VLS process, the metal catalyst film should be annealed above the melting-point temperature to transform into separated droplets, meanwhile, the high temperature (typically 600–1100 °C) can decompose the precursor gas, for example, the silicon tetrachloride ($SiCl_4$), or silane (SiH_4), which will be preferentially absorbed on the surface of the liquid droplets. When the Si atom dissolves into the liquid droplets, a liquid eutectic alloy will be formed. With the continuously decomposed precursor molecules being absorbed, the catalyst droplets become supersaturated to overcome the nucleation barrier. Then, the continuous Si atoms begin

© 2024 Wiley-VCH GmbH

21951071, 2024, 9, Downloaded from https://advanced.onlinelibrary.wiley.com/doi/10.1002/adom.202302121 by Nanjing University, Wiley Online Library on [04/11/2026]. See the Terms and Conditions (https://onlinelibrary.wiley.com/terms-and-conditions) on Wiley Online Library for rules of use; OA articles are governed by the applicable Creative Commons License

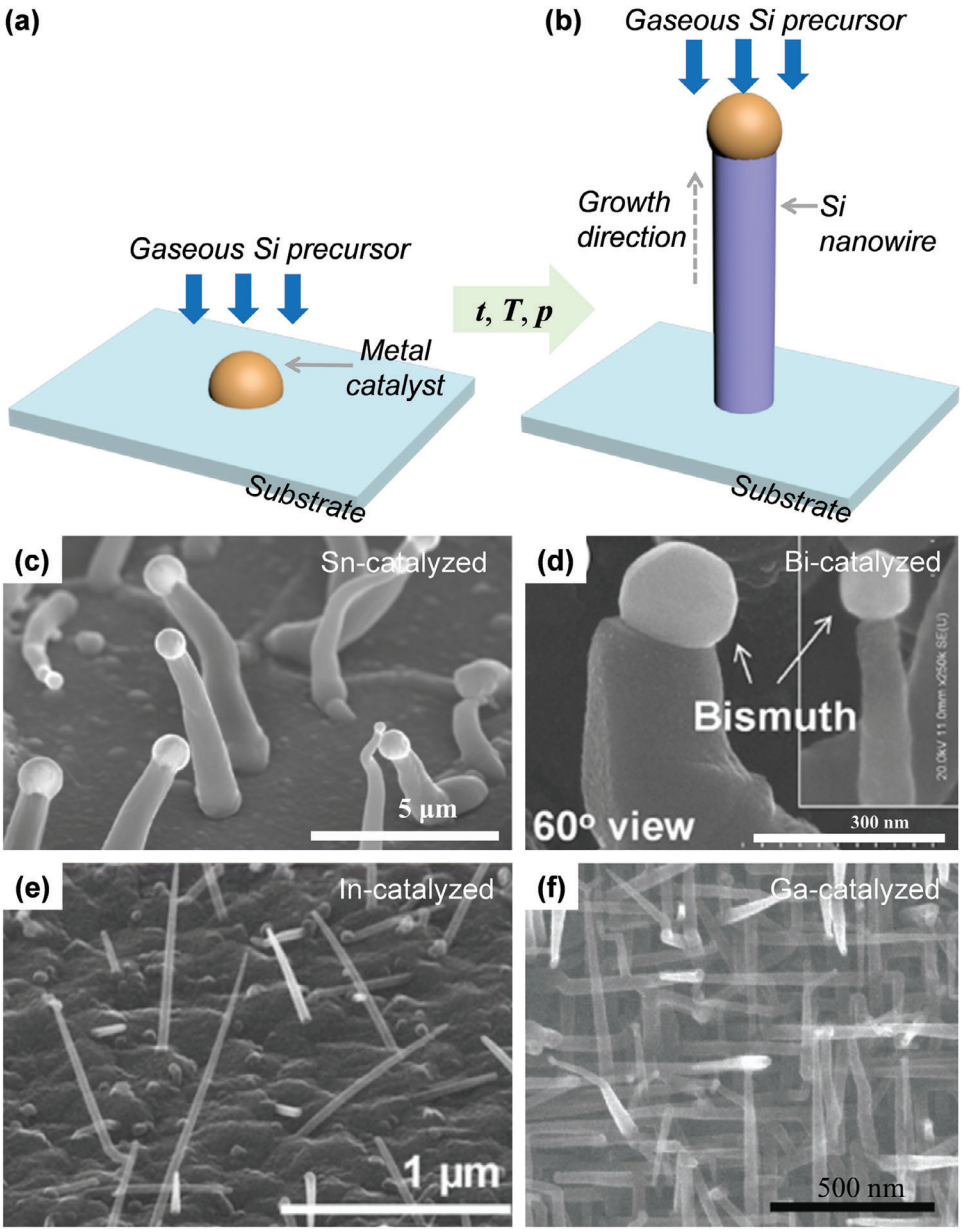


Figure 3. a,b) Schematic of the VLS growth mechanism ((a) catalyst droplets formed on the substrate, and b) growing SiNW using metal droplet). c) SEM image of the SiNWs grown on SnO_2 at 275 °C.[133] Copyright 2009 IOP Publishing. d) Sideview SEM image of the Bi-catalyzed SiNW.[134] Copyright 2012 American Chemical Society. e) Sideview SEM image of the In-catalyzed SiNW.[135] Copyright 2012 IOP Publishing. f) Top view SEM image of Ga-catalyzed silicon nanowires.[136] Copyright 2009 IOP Publishing.

to precipitate at the liquid–solid interface, leading to the growth of crystalline SiNWs.[128] However, the high temperature is an obstacle to the large-scale fabrication of flexible devices directly on low-cost flexible substrates in Roll-to-Roll technology. Besides, the commonly used Au catalyst will introduce mid-gap recombination centers in SiNWs, as well as Zn, Cu, Fe, Co, and Cr, and the remnant Au catalyst on the top of SiNWs is difficult to remove to avoid metal contamination.[128–130] Thus, it is hardly possible to use Au as a catalyst for photovoltaic device applications. Finding suitable LMP metal to catalyze a low-temperature VLS growth of SiNW and avoid deep impurity levels is important for integrating 3D SiNWs into industrial-scale mature PECVD techniques.[75,131,132]

Since 2008, L. Yu et al have successfully demonstrated a low-temperature VLS process, by using LMP metal tin (Sn), indium (In), gallium (Ga), bismuth (Bi), and their alloy as catalysts,[133,134,136–138] as shown in Figure 3c–f. Although the LMP metals usually have lower surface tensions (<0.5 N m^{-1}) smaller than γ_{Si} (γ_{Si} = 1.0–1.5 N m^{-1}),[128,139–143] the VLS growth of SiNW can be successfully catalyzed by these low-surface-tension (LST) metals. [133,136,137] Based on a cross-section analysis, L. Yu and his co-workers have examined the local tension-force-balance in

 © 2024 Wiley-VCH GmbH

21951071, 2024, 9, Downloaded from https://advanced.onlinelibrary.wiley.com/doi/10.1002/adom.202302121 by Nanjing University, Wiley Online Library on [04/11/2026]. See the Terms and Conditions (https://onlinelibrary.wiley.com/terms-and-conditions) on Wiley Online Library for rules of use; OA articles are governed by the applicable Creative Commons License

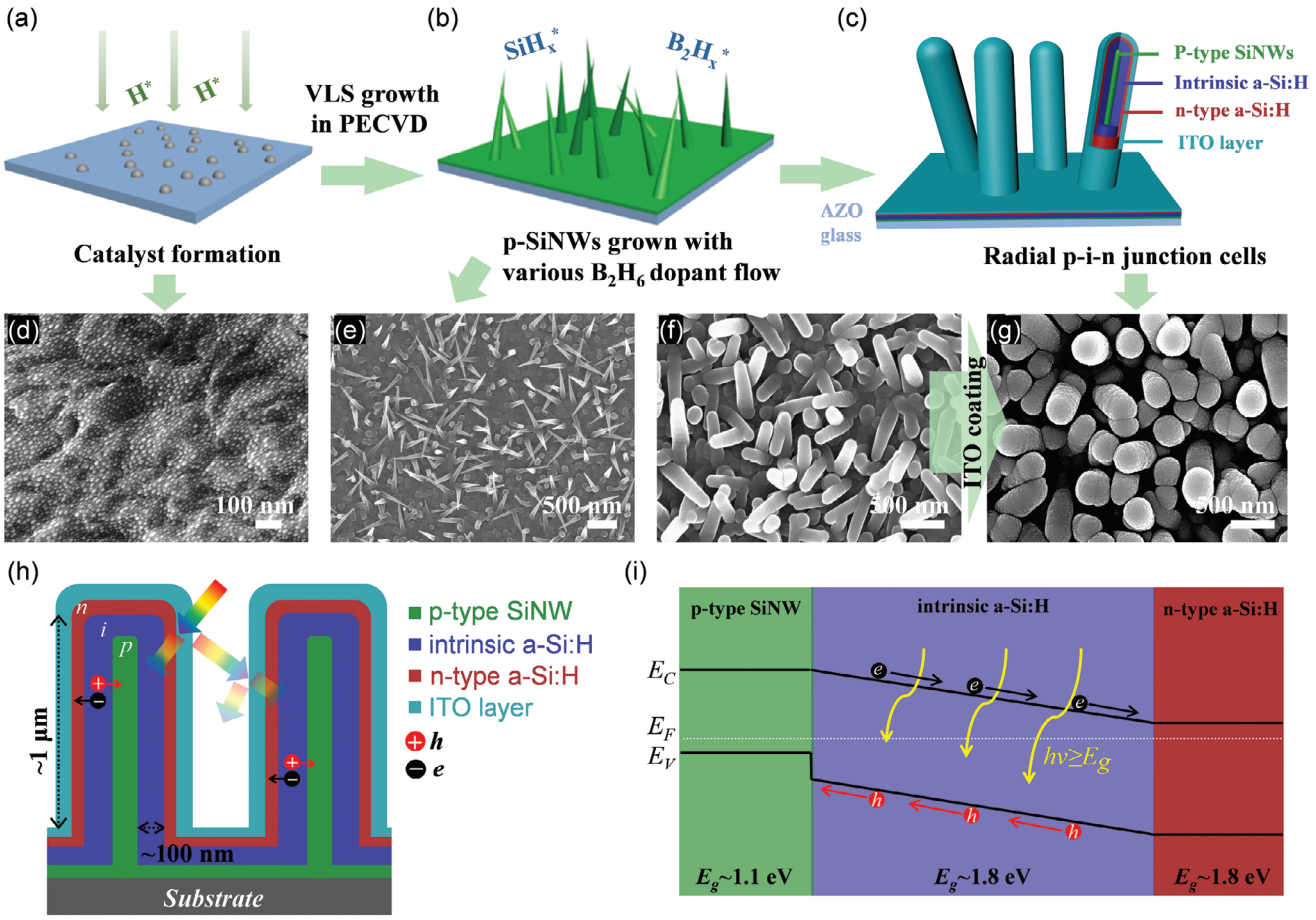


Figure 4. Illustrations of the fabrication process of RJ units: a) Sn catalyst formation, b) VLS growth of p-type SiNWs, and c) final RJ configuration, as well as the corresponding SEM images of d) Sn catalyst droplets after H_2 plasma treatment, e) p-type SiNWs, f) RJ units and g) final-fabricated RJ units with ITO coating.[79] Copyright 2019 Optical Society of America. h) Light absorption and carrier collection directions RJs. i) Band diagram of a-Si:H RJ unit at equilibrium.

a VLS process of growing SiNW by using Sn as a catalyst.[138] As a result, they found that an ultrathin sidewall-spreading LST-catalyst layer existed, which can help to establish the tension-force-balance in the vertical direction at the tripe-phase-line and stabilize the catalyst drop during growth. Thus, the SiNWs can be prepared at a low temperature down to 350 °C in a PECVD system, which makes it possible to fabricate SiNWs directly on the flexible substrates, helping to fabricate robust and mechanically stable flexible thin film optoelectronics with very high power-to-weight ratio.[77,78] Moreover, the impurity levels, which are introduced by these LMP-metal catalysts, are far away from the middle of the bandgap of c-Si, as well as the residual catalyst can be completely removed by H_2 plasma treatment, which will not cause a negative effect on the performance of a-Si:H RJ thin film photovoltaics.

2.2. Device Fabrication and Working Mechanism

The fabrication procedures of the a-Si:H RJ solar cells upon Al-doped zinc oxide (AZO) coated glass substrates are schematically illustrated in **Figure** 4a–c. First, a Sn layer with a thickness of 4 nm was thermally evaporated on the substrate, and then it was exposed to H_2 plasma for 5 min at 200 °C in the chamber of PECVD. The flow rate, the RF power density, and the chamber pressure were fixed at 20 SCCM, 10 mW cm^{-2}, and 30 Pa, respectively, to form discrete Sn droplets and remove the surface oxide layer, as shown in Figure 4d. Then, 60 SCCM H_2, 6 SCCM SiH_4, and 1.8 SCCM B_2H_6 were introduced as precursor gases to grow p-type SiNWs via an Sn-catalyzed VLS process, and the substrate temperature, the RF power density, and the chamber pressure were fixed at 350 °C, 20 mW cm^{-2}, and 100 Pa, respectively, for 15 min. Next, the temperature was decreased to 150 °C, and an intrinsic a-Si:H layer was coated around the VLS-grown SiNWs, by introducing a mixture of 20 SCCM H_2 and 6 SCCM SiH_4, for 60 min. Subsequently, an n-type a-Si:H layer (≈10 nm thick) was deposited, by adding 2.6 SCCM PH_3 dopant gas. At last, an ITO layer was prepared by magnetron sputtering through a shadow mask to form the top transparent electrodes. Figure 4c presents a final radial multilayer junction. Figure 4e–g show the SEM images of the VLS-grown p-type SiNWs, *p-i-n* RJ units, and RJ units coated with ITO layers, respectively. More experimental details are available in our previous work.[76,134,144] The a-Si:H RJ units deposited around SiNWs not only bring the advantage of

© 2024 Wiley-VCH GmbH

21951071, 2024, 9, Downloaded from https://advanced.onlinelibrary.wiley.com/doi/10.1002/adom.202302121 by Nanjing University, Wiley Online Library on [04/11/2026]. See the Terms and Conditions (https://onlinelibrary.wiley.com/terms-and-conditions) on Wiley Online Library for rules of use; OA articles are governed by the applicable Creative Commons License

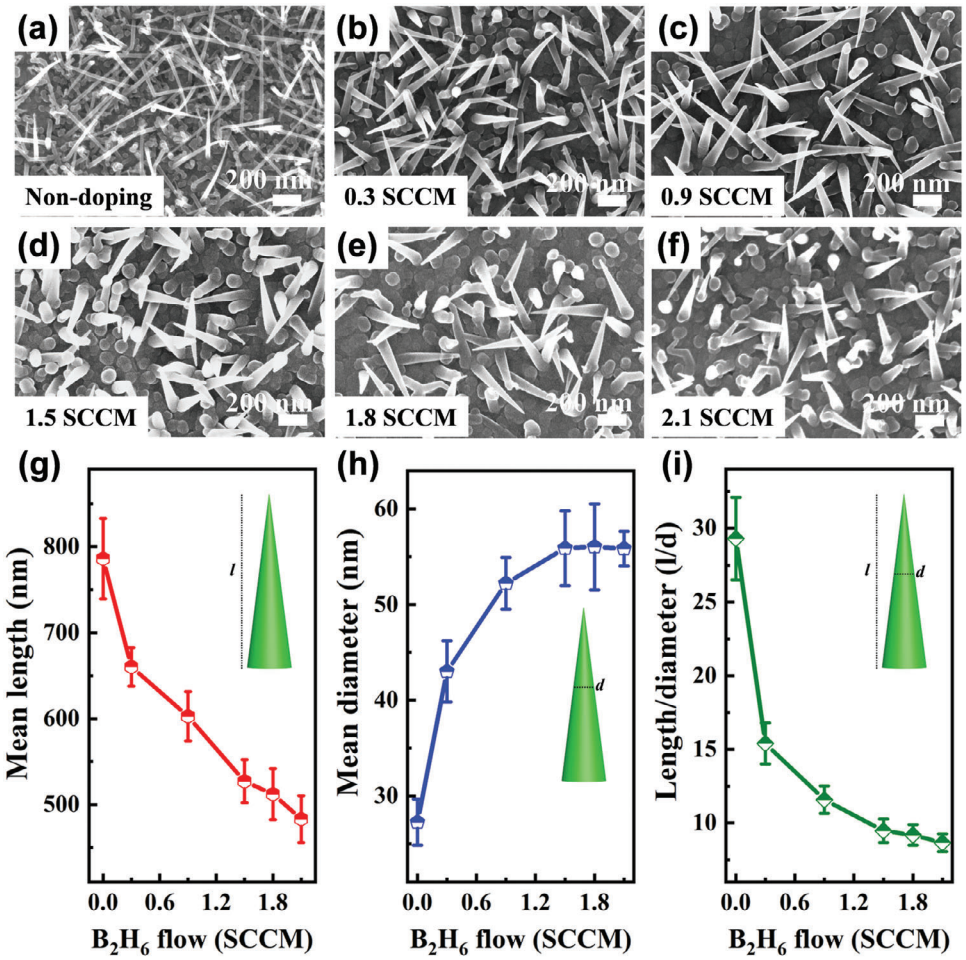


Figure 5. a–f) SEM images of the p-type SiNWs prepared under different B_2H_6 flow rates ranging from 0 to 2.1 SCCM, and g) the length l_{nw}, h) the diameter d_{nw} (extracted roughly at the middle of SiNWs) as well as i) the aspect-ratios $r \equiv l_{nw}/d_{nw}$, respectively.[79] Copyright 2019 Optical Society of America.

excellent light trapping but also orthogonalize the carrier collection and light absorption directions (Figure 4h). Besides, the RJ units can be fabricated very thin to strengthen the built-in field, ensuring a more efficient collection of carriers. Figure 4i shows the band diagram of the RJ photovoltaic devices at equilibrium, where E_F, E_V, and E_C are the Fermi energy level, the top of the valence band, and the bottom of the conduction band, respectively. As the incident light goes through the top ITO layer, photocarriers are generated in the ultrathin intrinsic a-Si:H absorber layer, and then separated by the built-in electric field of the *p-i-n* junctions. Thus, to seek a higher performance of RJ solar cells, both the geometry (for better light harvesting) and the doping control (for higher *p-i-n* junction quality) of the 3D SiNW framework are important.

2.3. Coupling Effect of Doping and Geometry on Performance

Recently, S. Zhang et al have demonstrated that when the diborane (B_2H_6) is used as a dopant to fabricate p-type SiNWs, a coupling between geometry and doping effect can be observed, emphasizing a commonly neglected but crucial aspect in fabricating high-performance RJ thin film solar cells.[79] **Figure 5** shows the SEM images of p-type SiNWs prepared using B_2H_6 as dopant gas with different flow rates ranging from 0 to 2.1 SCCM, respectively, as well as the length l_{nw} (Figure 5g), the diameter d_{nw} (Figure 5h, measured roughly at the middle of SiNWs), and their aspect ratios $r \equiv l_{nw}/d_{nw}$ (Figure 5i), which present a trend that the introduction of B_2H_6 leads to apparent geometry variation of the SiNWs. As the B_2H_6 flow rate increases, the SiNWs become shorter and thicker, with the length decreasing from ≈800 to ≈480 nm and the diameter increasing from <30 to ≈56 nm, as well as the density of SiNWs decreases apparently by 35%. As known, both the length and the density are crucial geometric factors to adjust the light trapping effect realized among the vertical-standing SiNWs or RJ units. Therefore, the influence of these geometry changes caused by boron doping is non-negligible on the performance of the RJ-structured photovoltaic devices.

The result of the different SiNW geometries, induced by increased B_2H_6 doping, was explored according to the photovoltaic performances of the SiNW-supported RJ solar cells. **Figure 6** shows the *J–V* curves of the RJ cells fabricated with different

© 2024 Wiley-VCH GmbH

21951071, 2024, 9, Downloaded from https://advanced.onlinelibrary.wiley.com/doi/10.1002/adom.202302121 by Nanjing University, Wiley Online Library on [04/11/2026]. See the Terms and Conditions (https://onlinelibrary.wiley.com/terms-and-conditions) on Wiley Online Library for rules of use; OA articles are governed by the applicable Creative Commons License

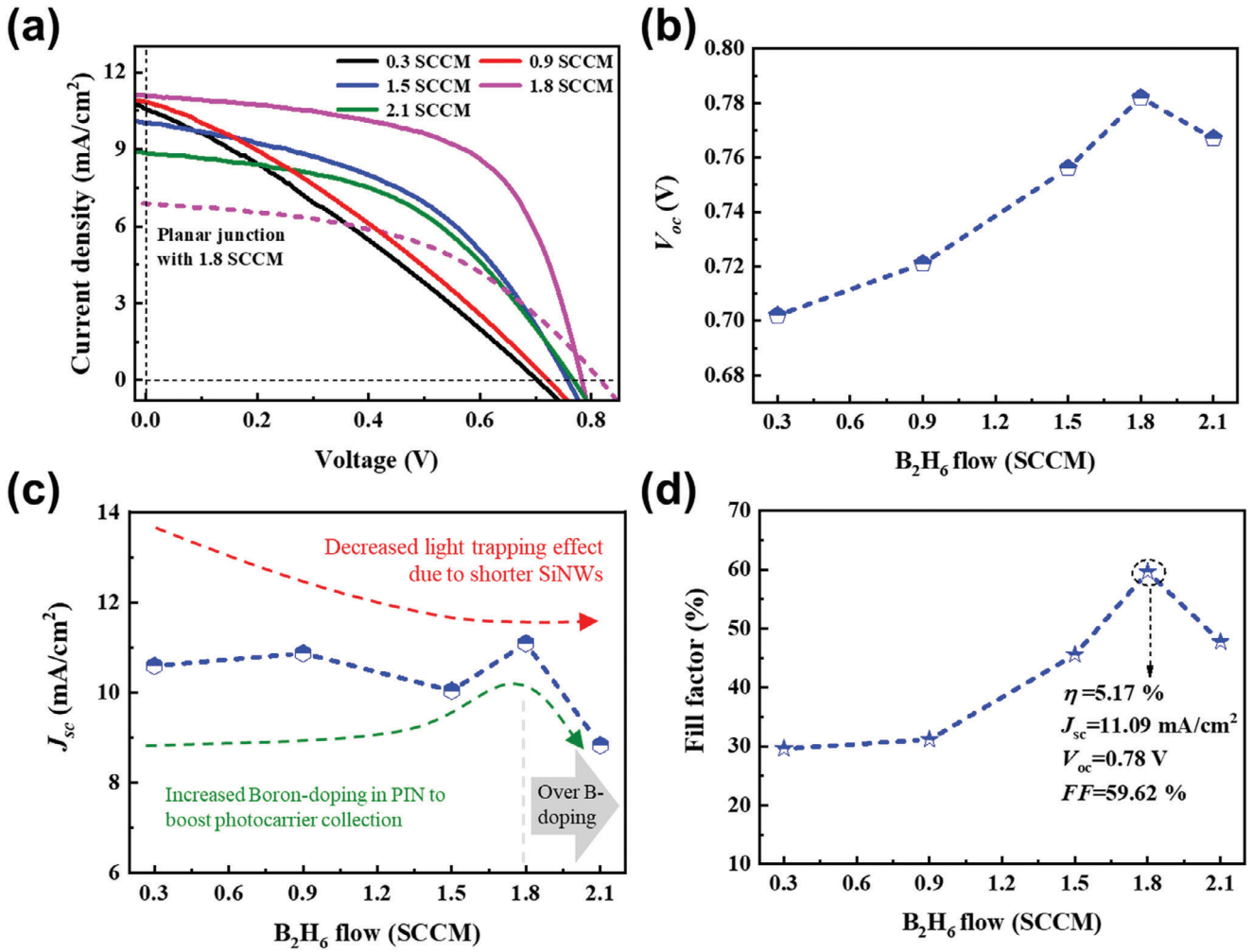


Figure 6. Measured *J–V* curves, V_{oc}, J_{sc}, and *FF* of the RJ units directly fabricated upon the p-type SiNWs using B_2H_6 as dopant gas with different flow rates.[79] Copyright 2019 Optical Society of America.

B_2H_6 flow rates, as well as the corresponding open circuit voltage (V_{oc}), short circuit current (J_{sc}), and fill factors (*FF*). As the flow rate of B_2H_6 rises from 0.3 SCCM to 1.8 SCCM, the value of V_{oc} increases from 0.70 to 0.78 V, while at an even higher B_2H_6 flow rate, it drops to 0.77 V, as well as a similar trend for the *FF*. These peaked trends of both V_{oc} and *FF* could result first from the increased p-type doping effect gradually built by the increased flow rate of B_2H_6, but only up to 1.8 SCCM, and then a higher flow rate would form the detrimental over-doping effect of boron dopants, which are known to polymerize at high concentration in Si matrix and lose doping effect.[145,146] As to the J_{sc}, it first augments slightly to ≈11 mA cm^{-2} at 0.9 SCCM B_2H_6 flow rate but decreases to 10 mA cm^{-2} at the dopant rate of 1.5 SCCM, then another peaked photo-current reaches 11.4 mA cm^{-2} at 1.8 SCCM, but followed by a rapid dropping <9 mA cm^{-2} when the B_2H_6 flow rate is higher. These observations indicate that 1) the photocurrent dips at 1.5 SCCM B_2H_6 are because of the boron-doping-induced geometry change of the RJ matrix (using B_2H_6 as dopant gas). 2) with the relatively low B_2H_6 flow rates, ranging from 0.3 to 0.9 SCCM, the stronger light absorption is contributed by the longer and denser SiNW matrices, but the photovoltaic performance in the *p-i-n* junctions is seriously limited by the insufficient doping in the SiNWs. 3) when the B_2H_6 flow rate is >1.5 SCCM, SiNW geometry changes slightly, but an enhanced doping effect in the RJ units can boost the overall device performance. Therefore, it is important to seek a proper trade-off between strong light trapping and sufficient doping for fabricating high-performance RJ thin film solar cells when using B_2H_6 as dopants.

3. Optoelectronic Properties

3.1. Impacts of Tilting and Arrangement of RJ on the Absorption

As we can see in the SEM image of **Figure 7a**, most of the RJ units are not upright standing, which is decided by the random orientations of the VLS-grown SiNWs. However, most of the works that have been reported were focused on a simplified state where the RJ units were in periodic upright standing postures,[83–85,147] which differs from the actual random orientations of RJ units. A full investigation of the light-harvesting performance of such tilted RJ units based on randomly oriented

© 2024 Wiley-VCH GmbH

21951071, 2024, 9, Downloaded from https://advanced.onlinelibrary.wiley.com/doi/10.1002/adom.202302121 by Nanjing University, Wiley Online Library on [04/11/2026]. See the Terms and Conditions (https://onlinelibrary.wiley.com/terms-and-conditions) on Wiley Online Library for rules of use; OA articles are governed by the applicable Creative Commons License

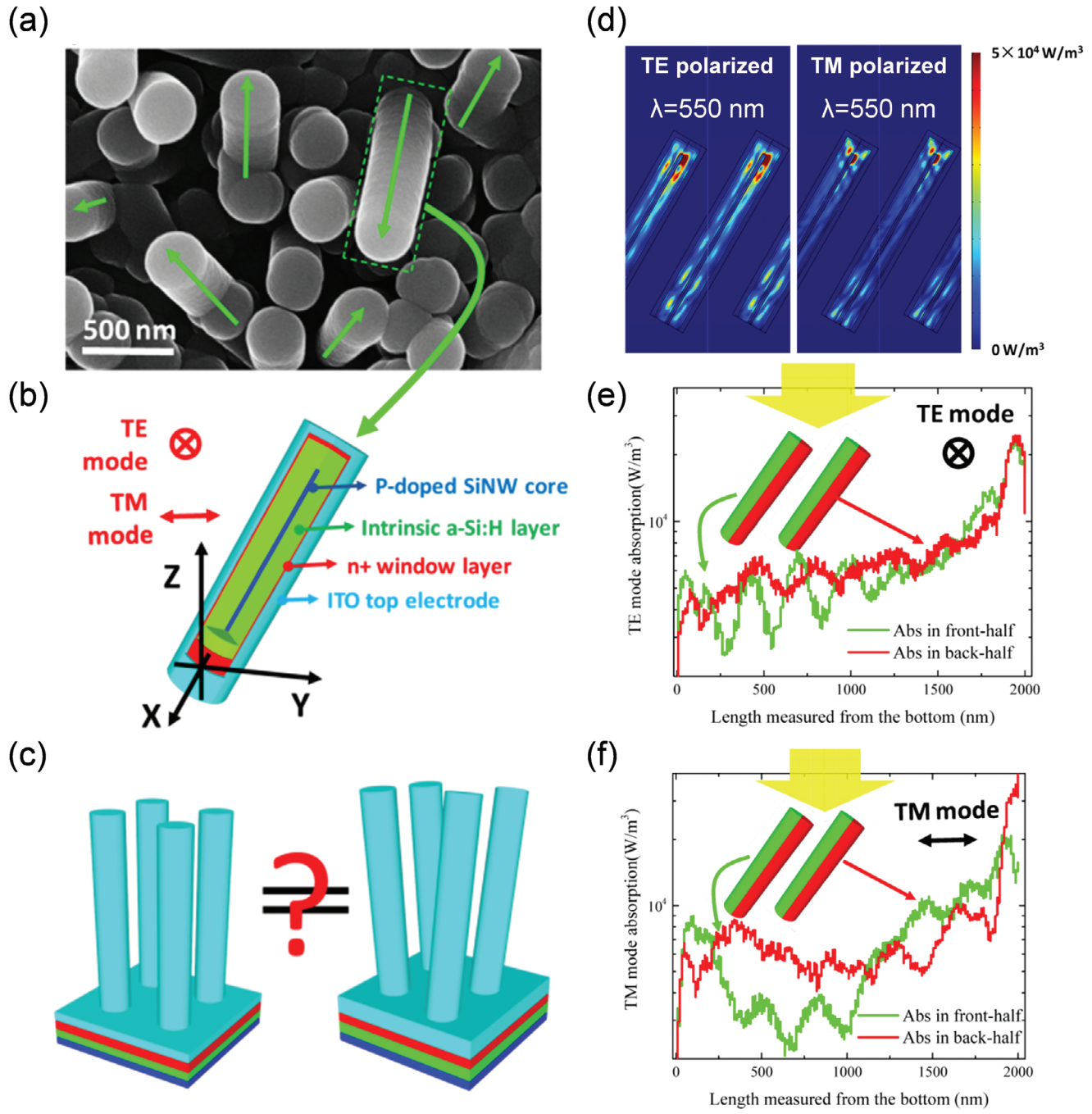


Figure 7. a) SEM image of the RJ units fabricated upon randomly oriented SiNWs grown by the VLS process, b) a diagrammatic sketch of the radially stacked multilayer structure, c) geometric arrangements of an upright standing (left) and an aperiodic random (right) RJ matrix, d) light absorption profiles realized within a 30°-tilted RJ array under TE mode and TM mode, as well as the absorption intensity distribution within the face-up half and the face-down half of the tilted RJ units, under e) TE and f) TM mode incidence.[148] Copyright 2015 Optical Society of America.

SiNWs is needed to provide a beneficial guide for experimental research. Thus, Lu et al have performed a theoretical simulation to investigate the influence of the tilting angles on the light absorption realized among the RJ units, considering different polarization and spatial separation conditions,[148] as shown in Figure 7b,c. Figure 7d shows the light absorption profiles of a tilted RJ unit (30°), with a non-uniform intensity of light absorption (incident light $\lambda = 550$ nm). It is interesting to note that the face-down halves that have experienced self-shadowing seem to have a better light harvesting behavior than that realized in the face-up halves, which is rather apparent in the top segments of RJs but is less prominent in the bottom segments. To quantify these observations, a range of volume integrations of the light absorption power have been performed, for the back face-down

© 2024 Wiley-VCH GmbH

21951071, 2024, 9, Downloaded from https://advanced.onlinelibrary.wiley.com/doi/10.1002/adom.202302121 by Nanjing University, Wiley Online Library on [04/11/2026]. See the Terms and Conditions (https://onlinelibrary.wiley.com/terms-and-conditions) on Wiley Online Library for rules of use; OA articles are governed by the applicable Creative Commons License

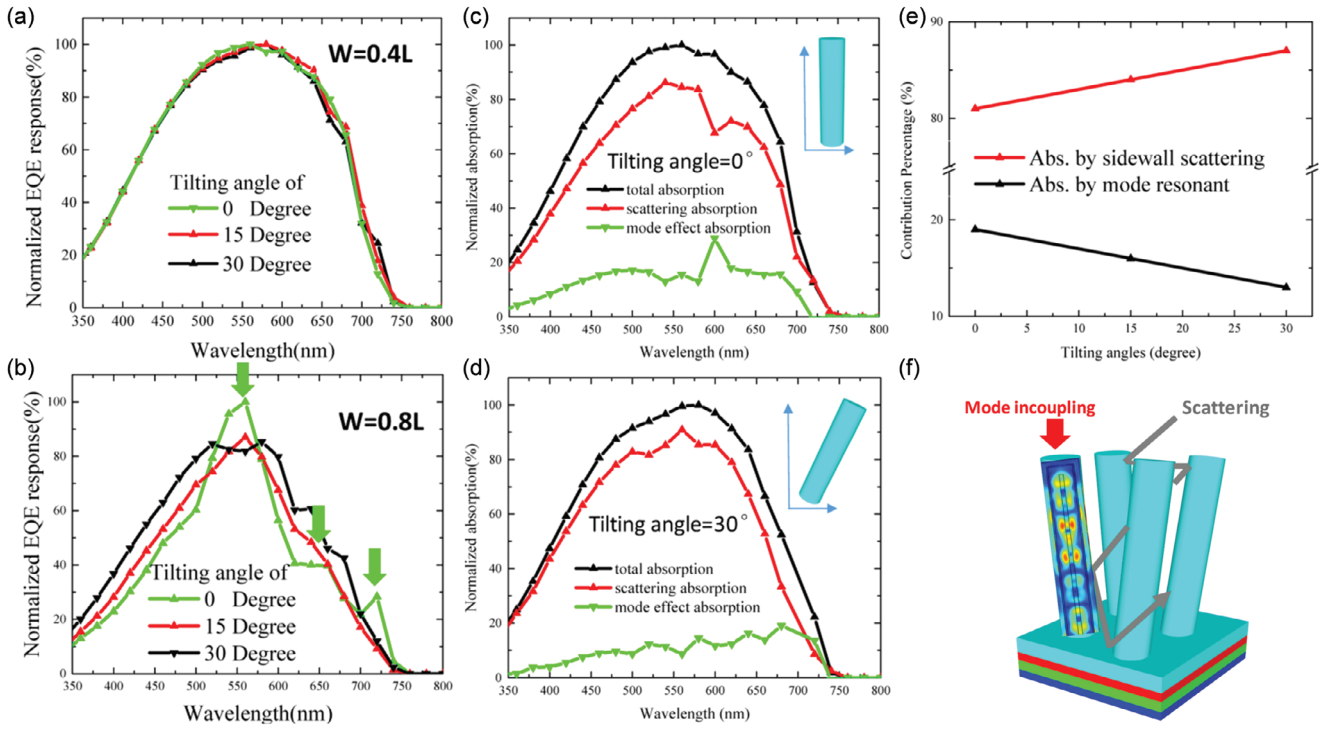


Figure 8. Normalized EQE curves (50–50 weighting for TE and TM mode) with a) an inter-cell spacing of $W = 0.4L$, and b) $W = 0.8L$, respectively (L represents the length of the RJ unit). Absorption response c) in an up-right standing RJ array and d) in a 30°-tilted RJ array, showing total absorption response (black), absorption realized in a scattering scenario (red), and absorption realized in a resonant mode in-coupling into the RJ units (green), as schematically illustrated in (f). e) The impact of the tilting angle on the light absorption realized in a scattering scenario and in a resonant mode.[148] Copyright 2015 Optical Society of America.

half (red curve) and front face-up half (green curve), measuring from the bottom to the top and under TE mode and TM mode, respectively, as shown in Figure 7e,f. In the lower segment that starts from the middle of the RJ unit, the face-down half even has a higher absorption than that of its face-up half counterpart, while under TM incidence a similar trend can also be observed in the face-down half for the top segment. It can be concluded that the self-shadowing effect has just an inconsequential impact on a tilting RJ matrix, but along the length of the RJ unit, the non-uniform light absorption profile does exist.

The EQE responses under different angles of $\theta = 0$, 15°, and 30°, which are gained with 50%–50% TE and TM mode weighted, are shown in **Figure** 8a,b, respectively, with different densities ($W = 800$ nm $= 0.4L_{RJ}$, and $W = 1600$ nm $= 0.8L_{RJ}$). For a dense RJ matrix ($W = 800$ nm $= 0.4L_{RJ}$, with a corresponding density of $\approx 2 \times 108/\text{cm}^2$), the tilting angle has negligible influence on the light absorption, however, in a sparser matrix ($W = 1600$ nm $= 0.8L_{RJ}$), the absorption curves with the tilting angle of 15° and 30° seem broader compared to that of the up-right standing situation (tilting angle = 0°). At the same time, as marked by three green arrows in Figure 8b, resonant absorption peaks appear at 550, 650, and 725 nm, respectively, for the up-right standing RJ units, but these peaks soon disappear or displace with increasing tilting angles. In other words, when the RJ matrix is dense enough, the tilting angle of the RJ unit may not be a critical parameter.

Within a randomly distributed RJ matrix (as shown in Figure 8f), there are two manners, that the incident light could interact with the RJ units: i) the incident light is captured and in-coupled into the resonant mode in a cavity-like RJ unit, and ii) the incident light scatters among RJ units and gets absorbed. To identify the contribution produced solely by the "resonant-mode-enhanced" absorption, the top end of the RJs is set as blocked or open condition to forbid or allow a resonant mode in-coupling into the RJs, to observe the difference in absorption realized under these two situations. As shown in Figure 8c,d, when the tilting angle is 0 or 30°, the contribution produced by the resonant mode just accounts for a small portion of <20%. The largest value of such contribution can be observed in an up-right standing configuration, and then monotonically decreases down to 12% with increasing tilting angles, as shown in Figure 8e. All these observations indicate that the "scattering-absorption" scenario plays a dominant role in accomplishing most of the light-harvesting, while the "resonant-mode-absorption" has a small influence.

3.2. Nanoscale Photovoltaic Responses in RJ Units

Understanding the effect of the resonant absorption or scattering on the light-harvesting behavior of the RJ units is critical to establishing a straightforward relationship between the 3D SiNW geometry and the light conversion performance. Recently, a laser excitation photoelectric microscope (LEPM) technology has been adopted by H. Zhang et al to directly detect the local light-harvesting behavior and photoelectric signals of RJ units with a smaller size of 4 μm wide,[149] as presented in **Figure** 9a, as

© 2024 Wiley-VCH GmbH

21951071, 2024, 9, Downloaded from https://advanced.onlinelibrary.wiley.com/doi/10.1002/adom.202302121 by Nanjing University, Wiley Online Library on [04/11/2026]. See the Terms and Conditions (https://onlinelibrary.wiley.com/terms-and-conditions) on Wiley Online Library for rules of use; OA articles are governed by the applicable Creative Commons License

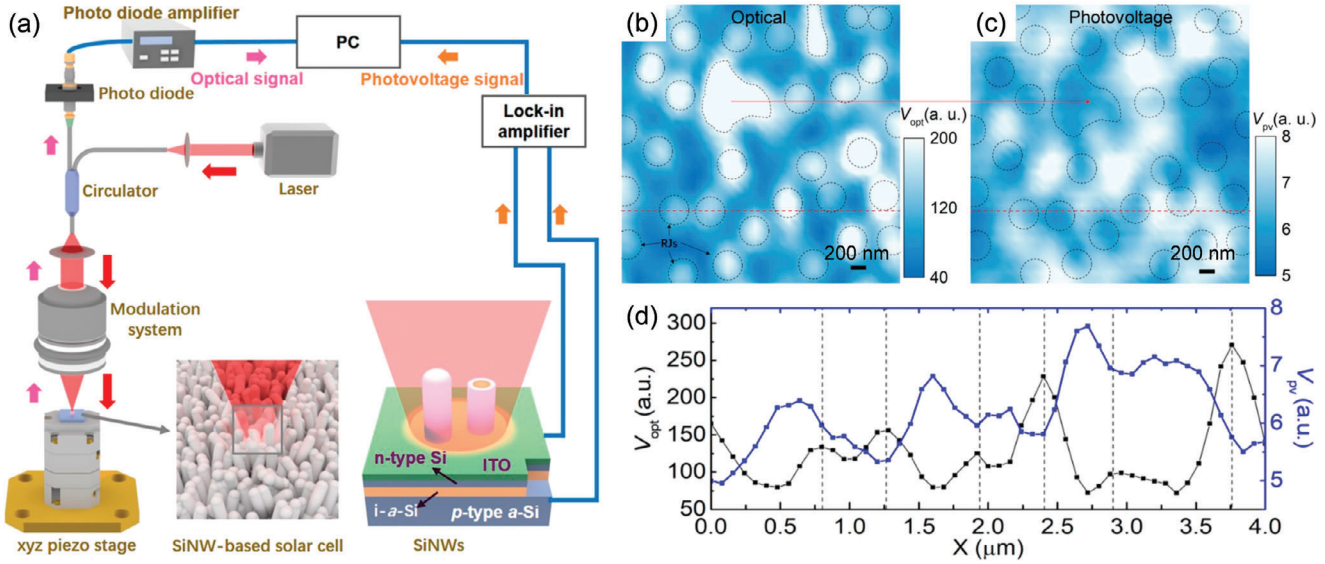


Figure 9. a) Diagram of laser excitation photoelectric microscopy (LEPM), b) detected optical and c) optoelectronic signals of a local region by using 405 nm laser as light source, and d) corresponding signal intensity.[149] Copyright 2019 American Chemical Society.

well as the measured optical and photoelectric responses shown in Figure 9b,c, respectively.

The reflected optical response can approximately decide the locations of the RJs because a stronger reflection at the top of the vertically standing RJ units can usually contribute to a brighter signal. However, most of RJ units are in tilted postures, which will be detected as elongated or irregular spots. As presented in Figure 9d, the highest photoelectric signals are commonly detected at the sites where the optical reflection responses are lowest. This suggests that the strongest absorption and photovoltaic generation are not realized over the standing RJs as normally expected in our previous work.[148] Instead, the highest photovoltage responses are generated in the so-called void region among RJ units.

To comprehend this funny correlation phenomenon, an RJ model has been built in the RF module of COMSOL Multiphysics to simulate the light absorption distribution of a single RJ cell, as shown in **Figure 10**. Figure 10c shows a mapping of the COMSOL-simulated effective light absorption of a single RJ unit, indicating that the highest absorption can be accomplished not over the RJ unit but rather at the positions 100–300 nm away from the center of the RJ, consistent with the experimental results obtained using LEPM technology. The curve of power absorption that can present this spatial deviation has been plotted against the distance from the RJ unit center, as shown in Figure 10d, by integrating/averaging the light absorption within the same distance from the RJ center, showing the highest absorption is located at ≈250 nm. Such a curve at least qualitatively explains why the highest photovoltaic responses are not achieved directly over the RJ units. Also, the simulated light absorption distribution presents a fact that the highest absorptions are always located at both sides of the tilted RJ unit, which are well consistent with that of the upright standing RJ units. These results indicate that the highest absorption of incident light is accomplished indeed in the nearby region surrounded by the standing RJ units, rather than in the overhead locations. Also, the influence of the light trapping effect among the 3D RJ units can be evaluated by varying the pitch of the RJs, which is equal to changing the RJ-unit density. The RJ matrix becomes very sparse with an increasing pitch to 3000 nm, which results in a rapidly diminished light-trapping effect, thus the highest light absorption response region reverts back to overlap with the RJ. When a singly placed RJ unit is under the same spotlight illumination, the strongest absorption of incident light is indeed achieved just over the RJ unit, not being in the nearby regions, which is caused by a much larger *p-i-n* junction volume coated upon the standing SiNW. However, the light absorption achieved by the single RJ is only 1/3 of that achieved by the RJ unit located in a matrix, which directly reflects the contributions of the light-trapping effect among the RJ units. These results also suggest that, in comparison to the direct light in-coupling into the RJ units at the top end, the light trapping and absorption among RJ units is more efficient.

4. Flexible Optoelectronics and Bio-Applications

4.1. Flexible RJ Thin Film Solar Cells on Al Foil

In recent years, flexible and lightweight solar cells/photodetectors with a high PTWR have attracted much attention for their remarkable capabilities in wearable and biomimetic/bio-friendly applications.[22,150–153] Recently, X. Sun et al have successfully demonstrated an exceptionally robust a-Si:H RJ solar cell on ultrasoft, ultrathin, and lightweight Al foil,[77] where the discrete and firmly standing SiNWs can act as firmly anchor sites to host the subsequently deposited amorphous thin films, as shown in **Figure 11**.

The *J*–*V* curves and corresponding V_{oc}, J_{sc}, *FF*, and η of the RJs on Al foil and AZO glass substrates as well as planar junctions on Al foil substrates were presented in **Figure 12**a,b, respectively. It is interesting to note that the RJs fabricated over the Al foil substrate generate a higher J_{sc} of 14.2 mA cm^{-2} than that of co-deposited RJ samples (J_{sc} = 11.2 mA cm^{-2}) constructed

© 2024 Wiley-VCH GmbH

21951071, 2024, 9, Downloaded from https://advanced.onlinelibrary.wiley.com/doi/10.1002/adom.202302121 by Nanjing University, Wiley Online Library on [04/11/2026]. See the Terms and Conditions (https://onlinelibrary.wiley.com/terms-and-conditions) on Wiley Online Library for rules of use; OA articles are governed by the applicable Creative Commons License

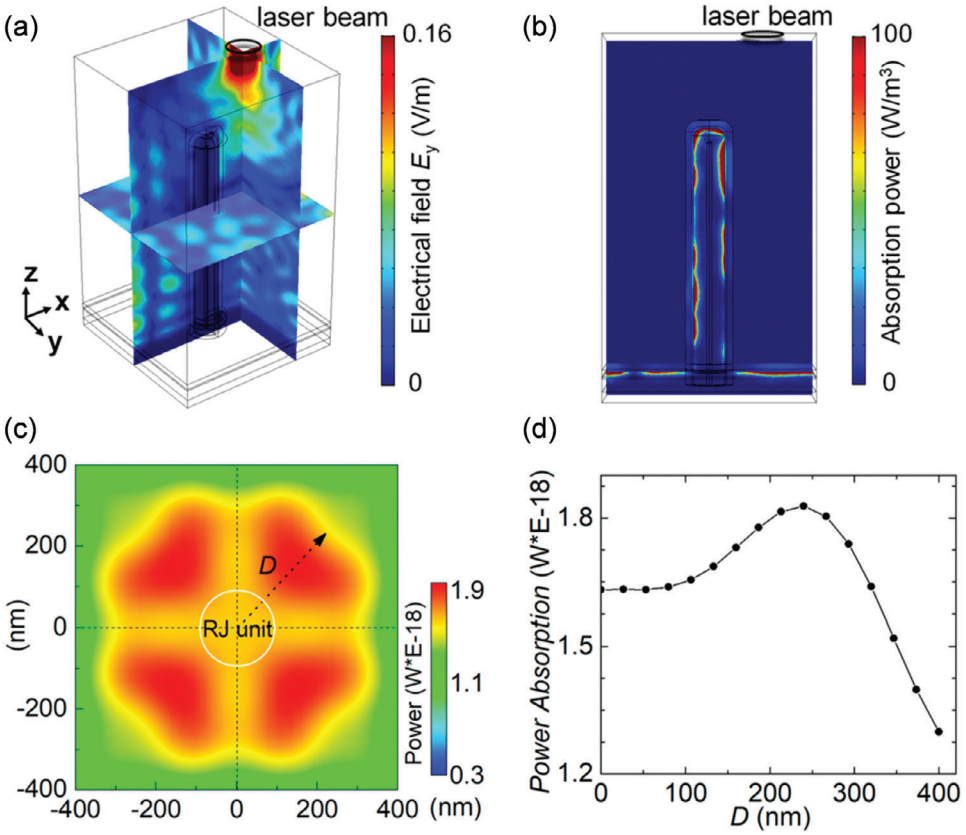


Figure 10. a) Sketch map of the built model of a single RJ unit at 405 nm light for COMSOL simulation, as well as the light field distribution presented by color cross profiles, and b) simulated light absorption profiles (the incident laser source is represented by the black circle out of the top border), and c) effective light absorption of a single RJ unit, and d) corresponding curves of integrated/averaged light absorption against the distance from the RJ unit center.[149] Copyright 2019 American Chemical Society.

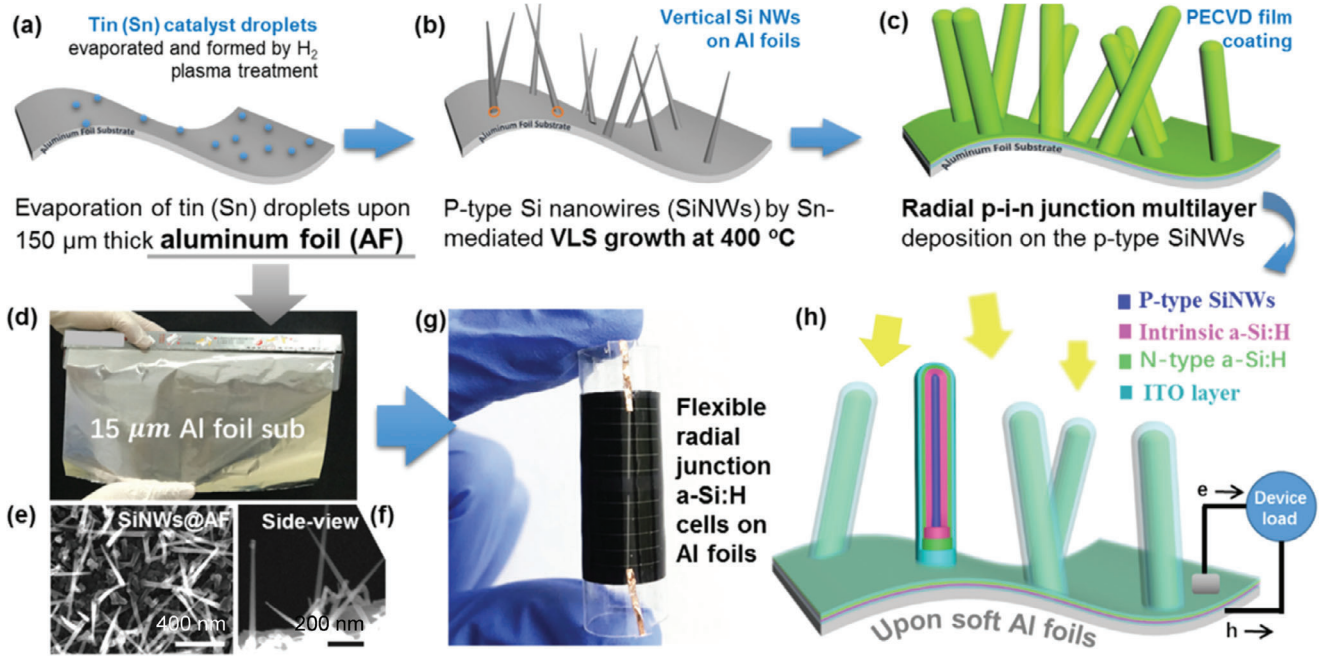


Figure 11. a–c) Sketch map of the fabrication process of RJ units on the surface of flexible Al foil, and h) radially stacked *p-i-n* multilayer structure of the final-fabricated RJ units, d) photo of the Al foil, e) top-view and f) side-view SEM images of the VLS-grown SiNWs on the Al foil, respectively, g) photo of flexible RJ solar cells encapsulated in EVA polymer layers.[77] Copyright 2018 Elsevier.

© 2024 Wiley-VCH GmbH

21951071, 2024, 9, Downloaded from https://advanced.onlinelibrary.wiley.com/doi/10.1002/adom.202302121 by Nanjing University, Wiley Online Library on [04/11/2026]. See the Terms and Conditions (https://onlinelibrary.wiley.com/terms-and-conditions) on Wiley Online Library for rules of use; OA articles are governed by the applicable Creative Commons License

21951071, 2024, 9, Downloaded from https://advanced.onlinelibrary.wiley.com/doi/10.1002/adom.202302121 by Nanjing University, Wiley Online Library on [04/11/2026]. See the Terms and Conditions (https://onlinelibrary.wiley.com/terms-and-conditions) on Wiley Online Library for rules of use; OA articles are governed by the applicable Creative Commons License

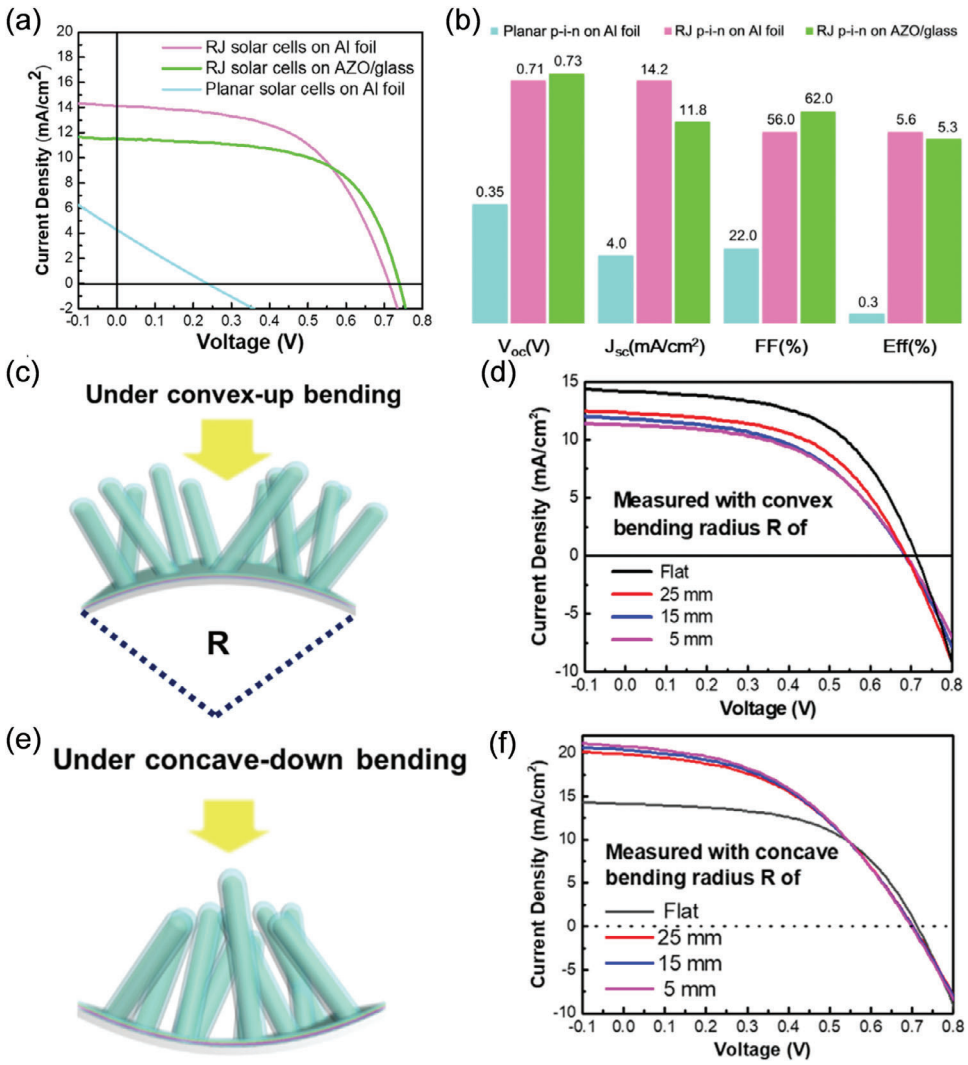


Figure 12. a) *J–V* curves measured under AM1.5G illumination, b) their corresponding performance parameters, c) sketch map of convex-up bending testing, and d) corresponding *J–V* curves with different radii, e) sketch map of concave-down bending testing, and f) corresponding *J–V* curves with different radii.[77] Copyright 2018 Elsevier.

on the glass substrate, which could be partially attributed to the favorable back-reflection provided by the Al foil substrate. Moreover, upon the rough and pliable Al foil substrate, the RJs can still deliver a V_{oc} of 0.71 V, which is only slightly lower than the value (V_{oc} = 0.73 V) achieved on the glass substrate. Meanwhile, the planar junction solar cells co-deposited on the same Al foil substrate just have a rather low V_{oc} of 0.35 V. These results emphasize the robustness of such 3D RJ structure in maintaining the integrity and functionality of the a-Si:H thin films deposited upon the surface of soft Al foil substrate. The flexibility of the RJ units fabricated on the Al foil substrate is examined by attaching them to cylinder rods (convex-up bending) or troughs (concave-down bending), with varying the radii from R_r = 5 mm to 25 mm, as presented in Figure 12c,e, respectively. Remarkably, the V_{oc} shows a rather stable trend just with a slight drop to 0.69 V, even after undergoing 300 times convex-up bending (with a very small radius of R_r = 5 mm). However, as the bending becomes larger and with more bending cycles, the J_{sc} exhibits a more obvious decrease. Therefore, the RJ solar cells can maintain a stable V_{oc} output and 71% of the initial PCE, even after bending with a very small radius (R_r = 5 mm). As to concave-down bending, it is interesting to find the measured J_{sc} increases significantly from 14 mA cm^{-2} to larger than 22 mA cm^{-2}, however, the V_{oc} decreases from 0.71 to 0.68 V. This abnormal increase of the J_{sc} could be simply attributed to the fact that the Al foil in concave bending state would act as like a mirror, which can concentrate the nearby incident light into the center region, improving the intensity of incident light. As a result, the samples demonstrate excellent robustness and flexibility that can sustain >200 cycles of concave-down bending to a 20 mm radius of curvature while retaining 80% of initial PCE.

More importantly, thanks to an overall PCE performance (η = 5.6%) and an ultralight Al foil substrate, an excellent PTWR of ≈1300 W kg^{-1} has been obtained in this work, which stands for an essential benefit for applying portable and wearable electronics. Besides, the fabrication cost of traditional planar a-Si:H

 © 2024 Wiley-VCH GmbH

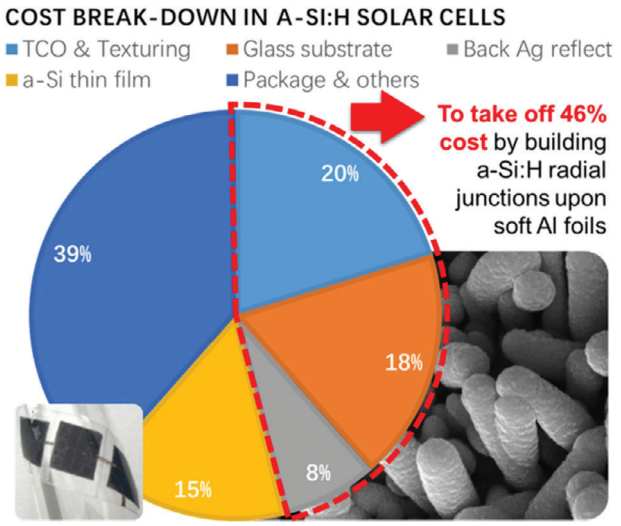


Figure 13. Fabrication cost reduction by ≈46% by RJ construction upon Al foil, compared to those in traditional a-Si:H module processing.[77] Copyright 2018 Elsevier.

thin film photovoltaic devices are usually made up of the following sections, such as TCO&texturing, glass substrate, back Ag reflector, and a-Si thin films, and package&others,[66–69,122,131] as shown in **Figure 13**. Because the Al foil substrate is very cheap and highly reflective and the excellent light trapping effect among 3D RJ units can be helpful for taking out the need for an extra TCO texture process and the back-reflection layer, the fabrication cost of 3D RJ solar cells directly upon Al foil substrates could be largely reduced down to only ≈54% of the original cost. This meaningful cost reduction, combined with outstanding flexibility and a very high PTWR, will be helpful for boosting the RJ a-Si:H thin film technology to serve as a very competitive approach to fabricating high power-to-cost flexible photovoltaics.

4.2. Tandem Structure for a Higher PTWR

By marrying advanced tandem junction design to the 3D SiNW framework, S. Zhang et al have successfully demonstrated a radial tandem junction (RTJ) thin film solar cell for the first time,[78] which consists of radially stacked *p-i-n* multilayers by using hydrogenated amorphous silicon germanium (a-SiGe:H) as inner light absorption layer and a-Si:H as outer light absorption layer, respectively. The RTJ solar cells were fabricated with a coaxial multilayer architecture of p-type SiNWs/intrinsic a-SiGe:H/n-type a-Si:H/p-type a-Si:H/intrinsic a-Si:H/n-type a-Si:H/ITO, as schematically drawn in **Figure 14a**. The a-SiGe:H thin film, which can be fabricated with a narrower and tunable bandgap (by adjusting the Ge content), allows a broader EQE response, as shown in Figure 14b, which can help broaden the light absorption spectrum.

The selected RTJ units were broken to expose the cross-sections, as seen for example in the SEM images presented in the left panels of Figure 14c,d. Intriguingly, due to the existence of slightly different contrasts between the inner and outer light absorption layers in the SEM images for the presence of Ge in the inner cell, the corresponding layer thicknesses are allowed to be extracted and verified. As presented by the counted data that is plotted in the right panels of Figure 14c,d, the outer a-Si:H absorber layer thickness is found to be around $t_{a-Si}^{outer} = 56 \pm 5$ nm, and the inner a-SiGe:H absorber layer thickness is around $t_{a-SiGe}^{inner} = 45 \pm 6$ nm, respectively, which are extracted from five samples at 149 different sites.

Based on an optimized SiNW structure and a series of critical fabrication parameter controls, the RTJ solar cells have been successfully demonstrated. The RTJ solar cells fabricated on the AZO glass can achieve a higher η of 8.1%, accomplished with a V_{oc} of 1.2 V, J_{sc} of 11.0 mA cm^{-2}, and *FF* of 61.5%, which can be largely better than that (η of 5.7%, V_{oc} of 0.8 V, J_{sc} of 12.4 mA cm^{-2}, *FF* of 58.6%) of the radial single junction units fabricated in the same batch, as shown in **Figure 15a,c**. Furthermore, the flexible RTJ units have been successfully fabricated in the experiment, as shown in Figure 15b, which were directly constructed upon ultrasoft, light-weight Al foil substrates, without any protection or separation layer between the RTJ and the surface of Al foil substrates. As shown in Figure 15c, the RTJ units on ultralight Al foil can accomplish a much higher η of 6.6% than that of 5.6% of radial single junction solar cells on Al foil.[77] Thus, combining the overall higher PCE performances with using a flexible and lightweight Al foil substrate, a much higher PTWR of ≈1628 W kg^{-1} has been successfully achieved, as shown in **Table 1**, as well as other published a-Si:H thin film solar cells. This figure of merit is especially crucial for boosting wearable/portable photovoltaic applications. Furthermore, it is also notable that this first experimental demonstration of RTJ photovoltaic devices upon VLS-grown SiNWs framework can achieve outstanding flexibility together with higher PTWR performance, which has not been possible for the traditional planar tandem structured photovoltaic devices.

4.3. Excellent Flexibility and Mechanical Stability

Figure 16a presents a typical side-view SEM image of RJ units directly grown on the surface of Al foil. The distribution of RJ units is found to be quite uniform, in spite of the curved surface and random stripes (marked using the white dashed lines), which are rather normal for commercial Al foil because of the standard twin-roll-casting process.[157] In comparison, the planar a-Si:H thin films directly deposited on the surface of the Al foil are very vulnerable to even slight bending of Al foil, causing large cracks and peeling off segments (as shown in Figure 16b), while the RJ units supported by SiNWs are found to be quite continuous and uniform after undergoing bending of flexible substrates,[77] as shown in Figure 16c. This observation provides a strong proof for the excellent mechanical stability of the 3D RJ units directly upon the ultrasoft Al foil. As shown in Figure 16d, the RJ units with random orientations are cross-linked with each other through the touching places at the top (marked by white dashed circles), providing an additional conductive top-crossing pathway at the top of the vertical-standing RJ forest, as highlighted by the white lines in the inset of Figure 16a and the yellow lines in Figure 16d. After convex-up bending (a very small radius of only 10 mm), as shown in Figure 16e, the bending-induced cracks appeared on the surface of the sample but spread only on the ground surface, rather than cutting through the standing RJ units.[126] An enlarged view of the cracked regions marked by green is pre-

© 2024 Wiley-VCH GmbH

21951071, 2024, 9, Downloaded from https://advanced.onlinelibrary.wiley.com/doi/10.1002/adom.202302121 by Nanjing University, Wiley Online Library on [04/11/2026]. See the Terms and Conditions (https://onlinelibrary.wiley.com/terms-and-conditions) on Wiley Online Library for rules of use; OA articles are governed by the applicable Creative Commons License

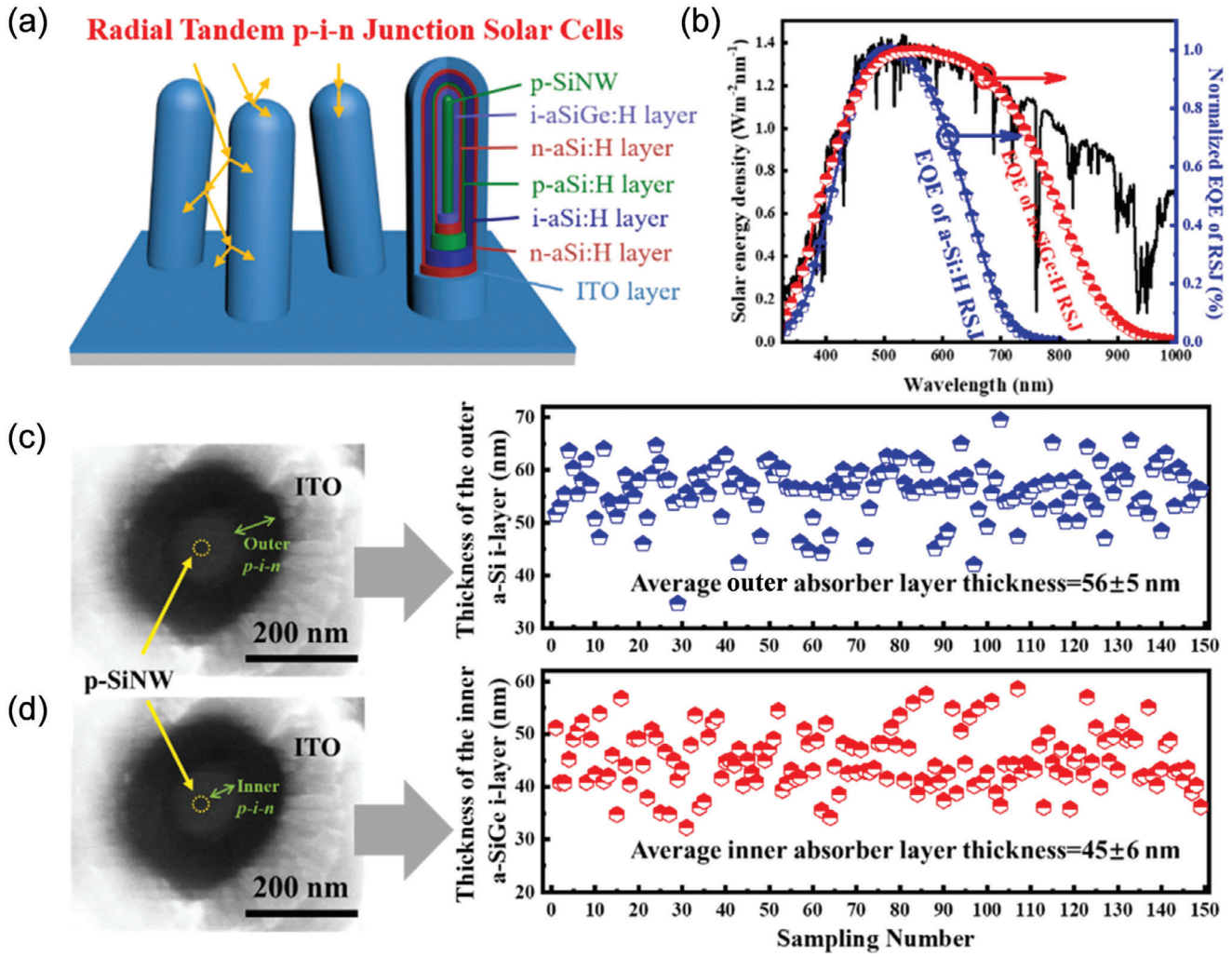


Figure 14. a) Finally fabricated RTJ configuration, b) solar spectrum, as well as normalized EQE curves of the a-Si:H and a-SiGe:H RJ units, and SEM images of the cross-section of the RTJ units are shown in the left panels of (c) and (d), respectively, and the counted thicknesses for outer and inner absorber layers are depicted in the right panels.[78] Copyright 2021 Elsevier.

sented in Figure 16f, and the width of cracks is counted and presented in Figure 16g, showing a value of ≈160 nm. It is noted that, after 1000 times convex-up bending, the 3D RJs can still touch their neighbors with no difficulty, spanning over these bending-induced irregular cracks to maintain the continuous top-crossing pathway (as marked by yellow lines shown in Figure 16f). Therefore, this 3D pathway feature allows a distinctive capability to overcome the detrimental effect of these bending-induced cracks to some degree, as marked by the pink rectangles in Figures 16e and 17a–c. These discrete standing RJs can also partly restrain the unidirectional or unlimited crack spreading, to prevent the formation of continuous and long cracks and separate the cracks into local and tiny ones, as presented in Figures 16f and 17d–h.

Using COMSOL analysis to carry out the finite element simulation of the vertical standing RJ units on the Al foil substrate, the convex-up bending induced stress distribution among the 3D structure is clarified. As marked in the cross-section profile shown in Figure 17i, the simulated von Mises stresses at the RJ-top (green), RJ-root (purple), planar surface (black), and SiNW-root (red) places are extracted and plotted against the tensile strain in Figure 17j. It is remarkable that the von Mises stresses found at the RJ-top places are 3–4 orders of magnitude smaller than those found at the RJ-root and on the nearby planar surface places, indicating that the out-of-plane RJ segments, supported by the vertical standing SiNW matrix, can be very well separated and protected from the stress-rich surface of flexible substrates. These above-mentioned unique features of 3D RJ construction can contribute to the excellent flexibility and mechanical stability of the RJ thin film photovoltaics that are directly fabricated on the flexible substrates, which is beneficial to fabricating comfortable electronics and enabling close contact with the soft skin surface.

4.4. Flexible and Degradable RJs as Stimulators for Photoelectric Cardiac Pacing

Cardiac pacemakers are essential medical tools to extend the lifespan of patients.[158,159] However, usual cardiac pacemakers are

© 2024 Wiley-VCH GmbH

21951071, 2024, 9, Downloaded from https://advanced.onlinelibrary.wiley.com/doi/10.1002/adom.202302121 by Nanjing University, Wiley Online Library on [04/11/2026]. See the Terms and Conditions (https://onlinelibrary.wiley.com/terms-and-conditions) on Wiley Online Library for rules of use; OA articles are governed by the applicable Creative Commons License

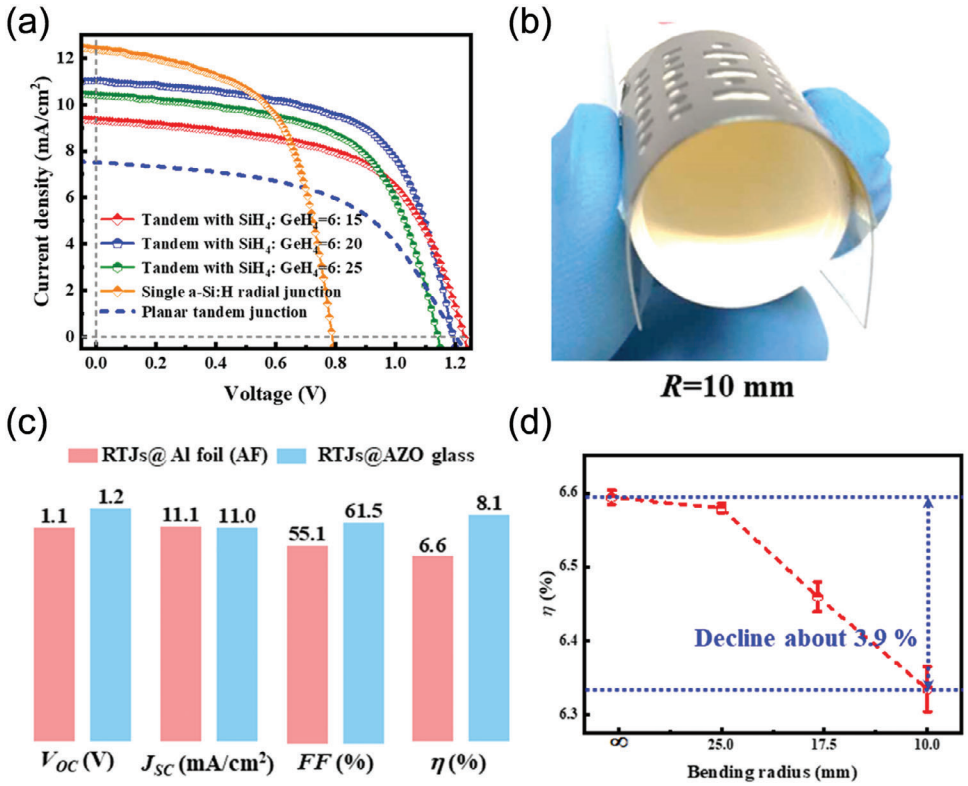


Figure 15. a) *J–V* curves of the RTJ units on AZO glass fabricated with different GeH_4 flows, respectively, compared to the planar tandem junction and radial single junction, b) photograph of convex-up bending, c) extracted performance parameters V_{oc}, J_{sc}, *FF*, and η of RTJ solar cells constructed on glass and Al foil, d) value of η of flexible RTJs versus different bending radius.[78] Copyright 2021 Elsevier.

bulky and rigid electronics and are powered by a battery,[160–162] which will limit their operation life, thus secondary installation or repair via surgery is needed, which will possibly cause infection and injury.[163] In a recent work,[22] Z. Liu et al have demonstrated a new strategy to accomplish heart pacing, as schematically drawn in **Figure 18c**, by using the self-powered flexible a-Si:H RJ photoelectric stimulator (as seen in Figure 18a,b), which can be conformally attached to the porcine heart, as shown in Figure 18e. Normally, the fabricated RJ units will be exposed on the top surface, with the outermost shell being an n^+-doped a-Si:H layer, thus the bottom of the Al foil substrate can be directly attached and contacted to the underlying heart surface, which will lead to an accumulation of positively charged hole produced from the *p-i-n* junction under light illumination, as shown in Figure 18d.

Using this kind of flexible self-powered a-Si:H RJ photovoltaics as photoelectric stimulators, a cardiac pacing experiment was performed on the porcine heart surface. The measured ECG signals are presented in **Figure 19a**, where the porcine heart is before, under, and after the stimulation carried out by the RJ stimulator, which is illuminated by the light source of a modulated laser at 650 nm (@ 2 Hz). It can be seen that the ECG peaks (as shown in Figure 19a) of the porcine heart have significant change when the light stimulation is carried out, compared to that of the normal condition, and when the light stimulation is removed, the ECG peaks can be recovered to its natural beating rate. Under

Table 1. Summary of the published a-Si:H thin film solar cells.

Substrate/Thickness (μm)	V_{oc} (V)	J_{sc} (mA cm^{-2})	PCE (%)	Power-to-weight ratio (W kg^{-1})	Ref.
PI/No data	≈0.8	≈1	3.2	200	[154]
Polyimide/20-30	6.5	1.6	5.8	340	[132]
Polyimide/20	14.0	≈0.5	≈4.4	275	[155]
Glass/1000	0.92	10.20	5.84	20	[156]
Graphene paper/53	0.87	11.96	5.86	8310	[156]
Al foil/15	0.71	14.2	5.6	1382	[77]
Al foil/15	1.1	11.1	6.6	1628	[78]

© 2024 Wiley-VCH GmbH

21951071, 2024, 9, Downloaded from https://advanced.onlinelibrary.wiley.com/doi/10.1002/adom.202302121 by Nanjing University, Wiley Online Library on [04/11/2026]. See the Terms and Conditions (https://onlinelibrary.wiley.com/terms-and-conditions) on Wiley Online Library for rules of use; OA articles are governed by the applicable Creative Commons License

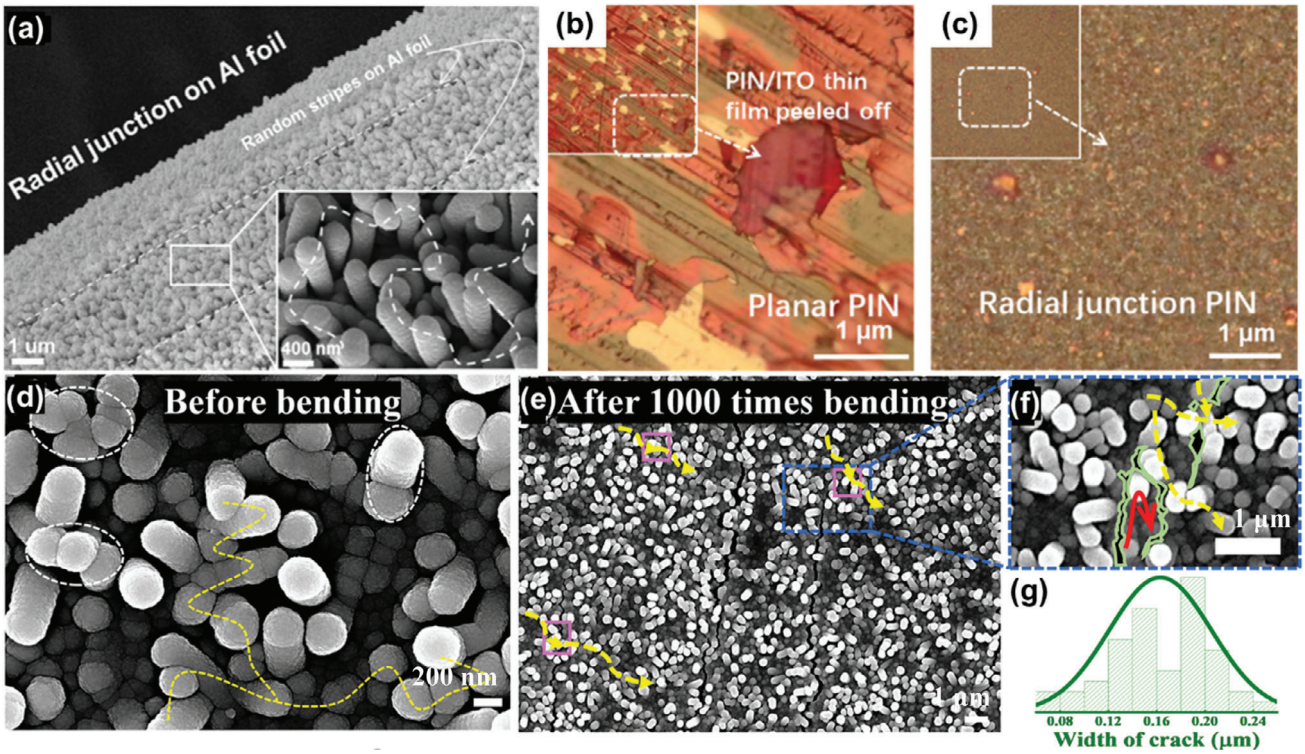


Figure 16. a) Side-view SEM image of RJs standing upon Al foil surface, as well as the inset image providing more details of the geometric features, b,c) microscope photos of the planar and RJ structure grown upon Al foil substrate, respectively.[77] Copyright 2018 Elsevier. d–f) SEM images of RJs on Al foil before or after undergoing substrate bending, and g) the counted width of cracks induced by convex-up bending.[126] Copyright 2022 Wiley-VCH GmbH, Weinheim.

the modulated laser illumination, the heart rate increased from ≈101 times min^{-1} (normal condition) to ≈128 times min^{-1} (under light stimulation), which effectively suggested that the flexible RJ stimulator can help control the heart beating.

The details of the detected ECG peaks in different conditions are extracted and presented in Figure 19b–d. It can be seen that the Q, R, S waves complex (QRS) has been largely modified under light stimulation, corresponding to ventricular depolarization that leads to the contraction of the left and the right ventricles. Compared to the normal condition, the laser-modulated RJ stimulator can result in a straightforward stimulation of the cardiomyocytes, which can further improve the amplitude of the R wave and decrease the duration of QRS, as shown in Figure 19c. The shorter QRS duration suggests a faster ventricular depolarization, which can be governed by the frequency of external light stimulations. This is also helpful in recovering the normal electrophysiology of patients with heart failure disease induced by ventricular hypertrophy or intraventricular block. These results indicate that the flexible RJ stimulator fabricated on the Al foil substrates has a significant potential to act as a direct pacemaker to govern heart-beating rates.

4.5. Flexible RJ NIR Photodetectors for Sphygmic Signal Monitoring

The heart rate is one of the most important physiological parameters, which can be used for extensive diagnostics and can be relatively easily detected by using the photoplethysmography (PPG) method, but not accurately because there is significant movement artefact or cardiac arrhythmia in pulse oximetry PPG techniques.[164–167] For a more accurate reflection of the heart beating, a direct measurement of the arterial blood volume change may be a better choice. The NIR probing light at ≈800 nm can penetrate deeper into the human skin/tissue.[168,169] Besides, it can be seen that the light absorption difference of oxyhemoglobin/deoxyhemoglobin variation almost disappears at the wavelength ≈800 nm (**Figure 20a**). In a recent work,[126] S. Zhang et al have demonstrated a rather flexible and robust RJ NIR photodetector directly upon Al foil substrates, using a-SiGe:H (≈1.4 eV) as the light absorption layer, which can greatly extend the light detection to the NIR wavelengths, thus allowing for an ultrafast sphygmic signal monitoring, as schematically drawn in Figure 20b.

By attaching the devices to cylindrical rods with different radii, ranging from R = 25 mm to 10 mm, as schematically drawn in Figure 20c, the flexibility of the RJ NIR photodetectors fabricated on the Al foil substrates was tested, and then the optoelectronic properties were measured after releasing from bending. The evolution of EQE (≈22%@800 nm) and the responsivity (≈140 mA/W@800 nm, deduced from the formulate $\text{Responsivity} = \frac{\text{EQE}(\%)\times\lambda}{100\times1240}$ [170]) with different bending radii and bending cycles are shown in Figure 20d,e, respectively, which remain almost the same even after undergoing 1000 times bending to a radius of only 10 mm.

© 2024 Wiley-VCH GmbH

21951071, 2024, 9, Downloaded from https://advanced.onlinelibrary.wiley.com/doi/10.1002/adom.202302121 by Nanjing University, Wiley Online Library on [04/11/2026]. See the Terms and Conditions (https://onlinelibrary.wiley.com/terms-and-conditions) on Wiley Online Library for rules of use; OA articles are governed by the applicable Creative Commons License

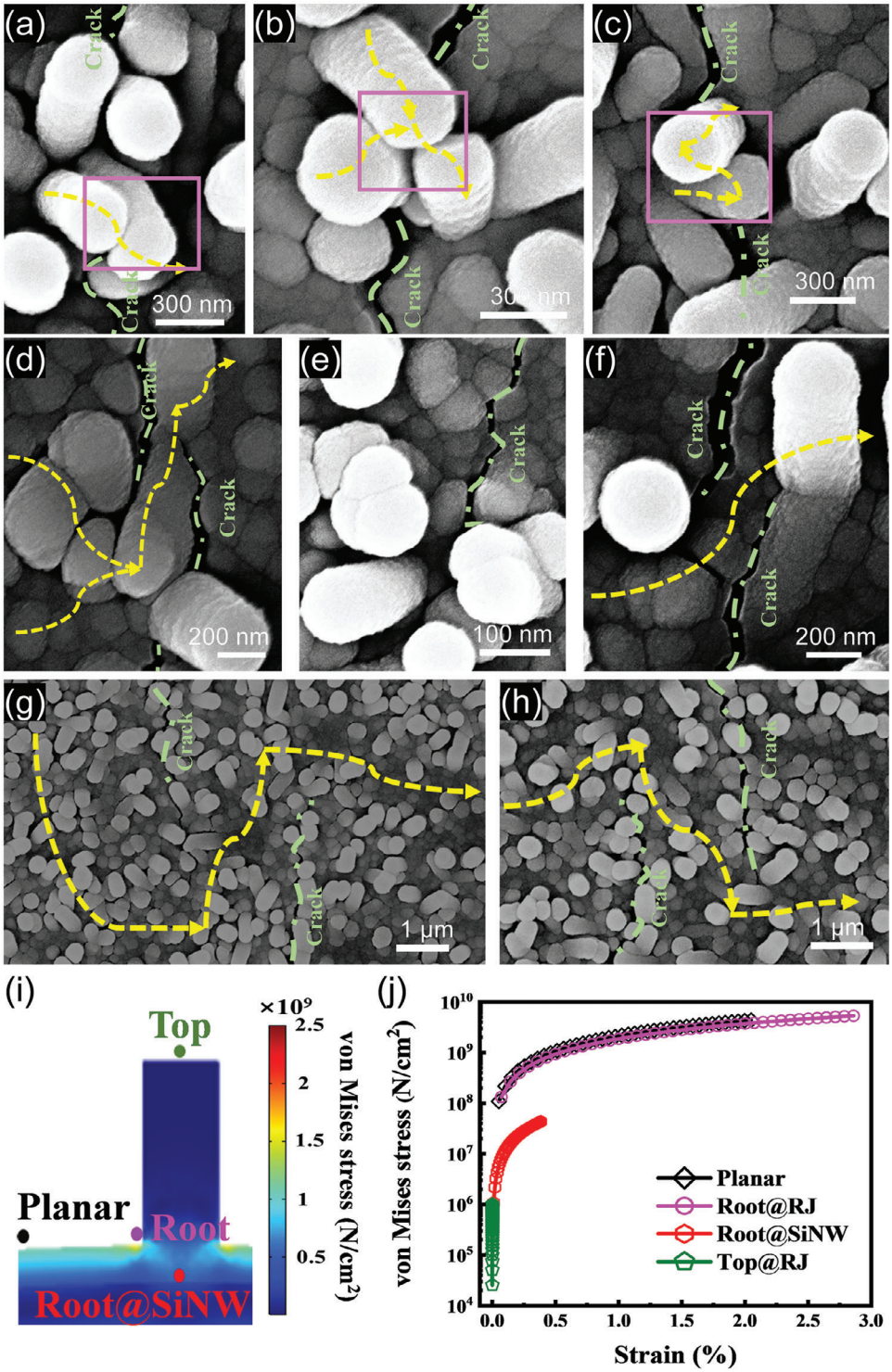


Figure 17. a–h) SEM images of the devices after undergoing convex bending of the substrate (green dash and dot lines represent crack), i) simulated von Mises stress distributions of RJ unit that undergoing convex bending, and j) corresponding curves of stresses versus strains.[126] Copyright 2022 Wiley-VCH GmbH, Weinheim.

© 2024 Wiley-VCH GmbH

21951071, 2024, 9, Downloaded from https://advanced.onlinelibrary.wiley.com/doi/10.1002/adom.202302121 by Nanjing University, Wiley Online Library on [04/11/2026]. See the Terms and Conditions (https://onlinelibrary.wiley.com/terms-and-conditions) on Wiley Online Library for rules of use; OA articles are governed by the applicable Creative Commons License

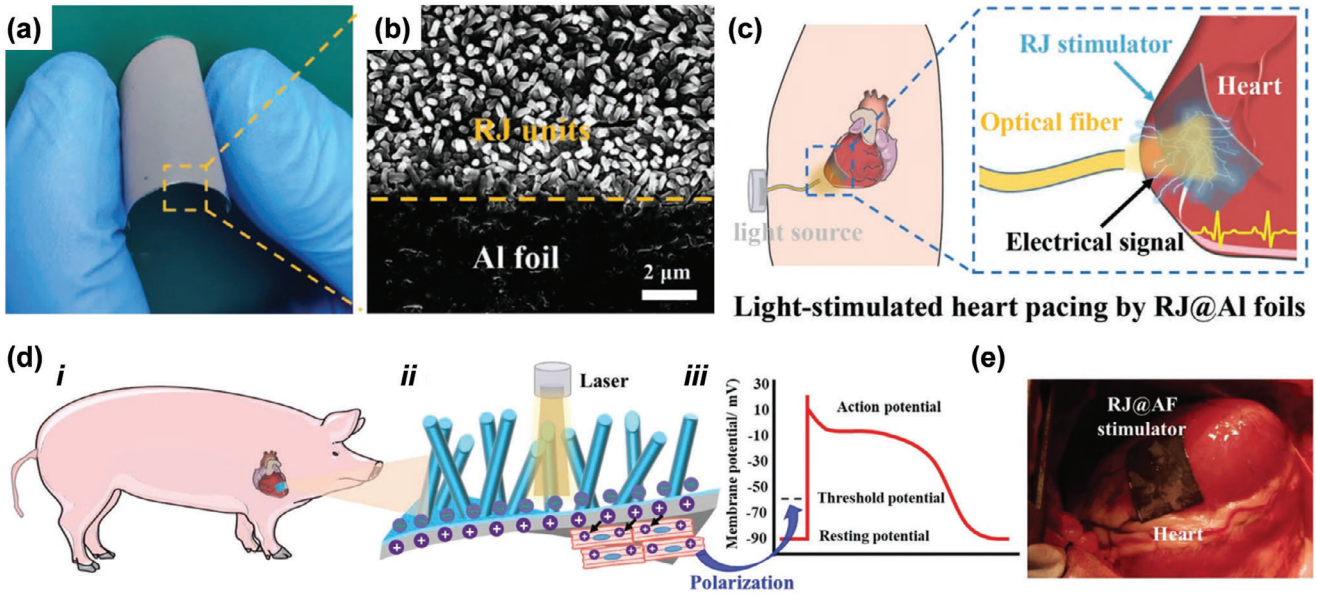


Figure 18. a) Photo of RJs on Al foil substrate, b) a cross-section SEM view, c) diagram of the a-Si:H RJ stimulator that is used for heart pacing, d) diagram of the arrangement of the living pig cardiac pacing experiment (with using the flexible RJ stimulator as pacemaker attached to the surface of pig heart), and e) the corresponding photograph of the experiment.[22] Copyright 2020 Wiley-VCH GmbH, Weinheim.

Then, as shown in **Figure 21**a, the subdermal pulse signals have been successfully captured by using the flexible RJ NIR photodetector as the PPG bio-detector that can be directly attached to the surface of the human wrist, where the arterial blood volume vibration is more obvious and easier to detect.[166] To verify the exclusion of oxyhemoglobin/deoxyhemoglobin variation as their absorption difference, the red and green light were used as probing light sources to detect the PPG signals, however, no

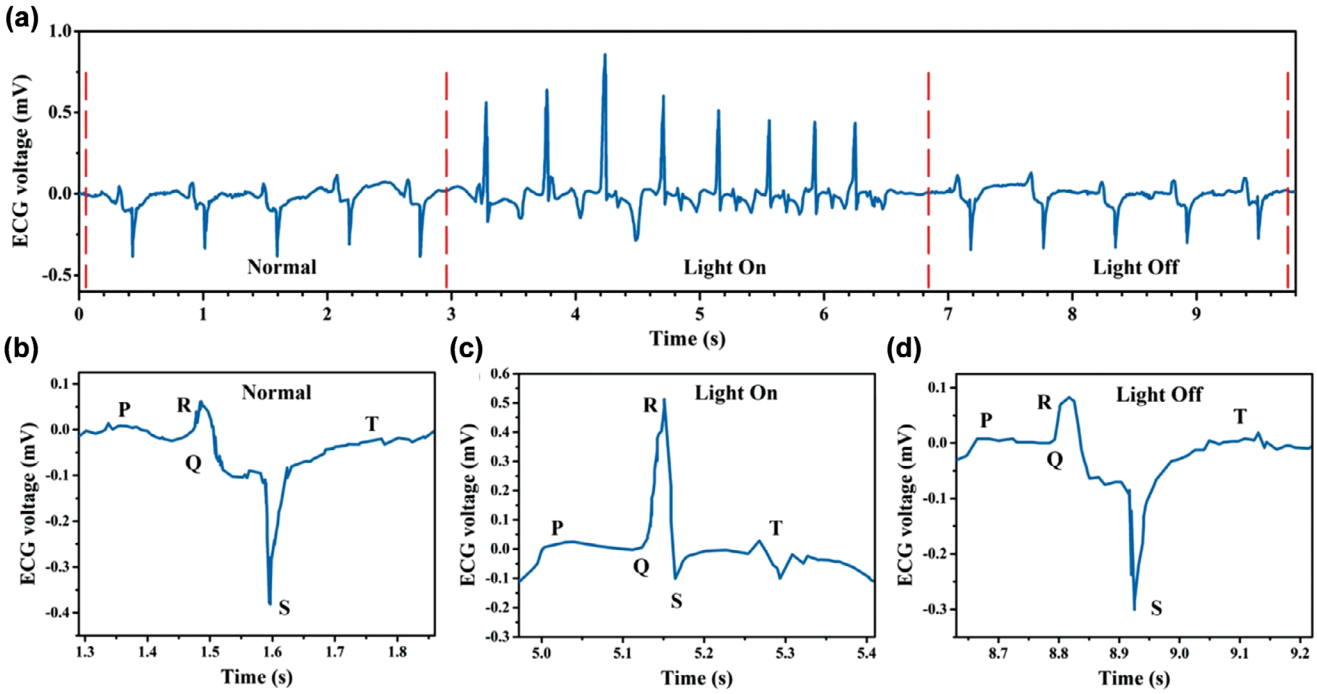


Figure 19. a) detected ECG signals before, under, and after external light stimulation, as well as b–d) enlarged views of the ECG details for corresponding distinct phases.[22] Copyright 2020 Wiley-VCH GmbH, Weinheim.

© 2024 Wiley-VCH GmbH

21951071, 2024, 9, Downloaded from https://advanced.onlinelibrary.wiley.com/doi/10.1002/adom.202302121 by Nanjing University, Wiley Online Library on [04/11/2026]. See the Terms and Conditions (https://onlinelibrary.wiley.com/terms-and-conditions) on Wiley Online Library for rules of use; OA articles are governed by the applicable Creative Commons License

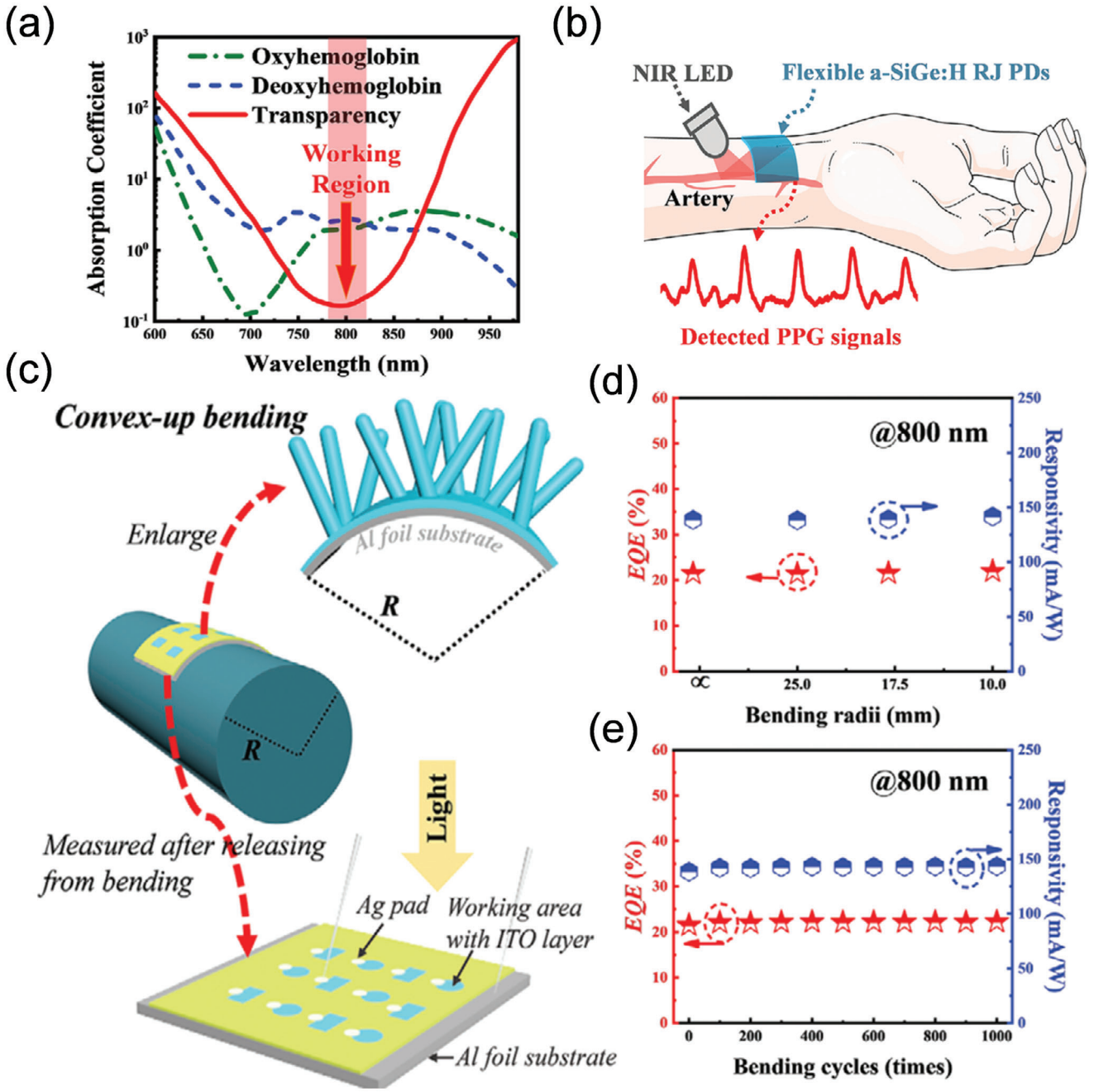


Figure 20. a) Absorption coefficient curves of deoxyhemoglobin and oxyhemoglobin in the blood of humans, b) diagram of detecting pulse at the wrist, c) diagram of convex-up bending and testing condition, and evolution curves of the values of EQE and responsivity at 800 nm with d) different bending radii and e) different bending cycles, respectively.[126] Copyright 2022 Wiley-VCH GmbH, Weinheim.

obvious sphygmic signals were detected, as shown in Figure 21c,e, for their limited penetration depth into the skin/tissue. Similarly, to further verify the detected signals are directly caused by the arterial blood volume change, we chose the back of the hand and arms as the detecting points, where the arterial blood volume change related to heart beating hardly exists, and no discernible PPG signals were detected by using a single NIR light source, as shown in Figure 21d,f. Thus, the clear and regular PPG signals, as shown in Figure 21b, can be efficiently achieved at the human wrist by using the NIR@~800 nm as a light source, which is certainly extracted from the variation of NIR light reflected/diffracted from the arterial blood volume change, directly caused by the heartbeats. Furthermore, the heart rate can be calculated to be 78 ± 5 beats per minute. These results suggest the flexible RJ NIR PDs developed herein can enable a reliable PPG heart rate detection technology by using a single NIR wavelength probing light source, which can help to chase and extract an accurate sphygmic signal via solely arterial blood

© 2024 Wiley-VCH GmbH

21951071, 2024, 9, Downloaded from https://advanced.onlinelibrary.wiley.com/doi/10.1002/adom.202302121 by Nanjing University, Wiley Online Library on [04/11/2026]. See the Terms and Conditions (https://onlinelibrary.wiley.com/terms-and-conditions) on Wiley Online Library for rules of use; OA articles are governed by the applicable Creative Commons License

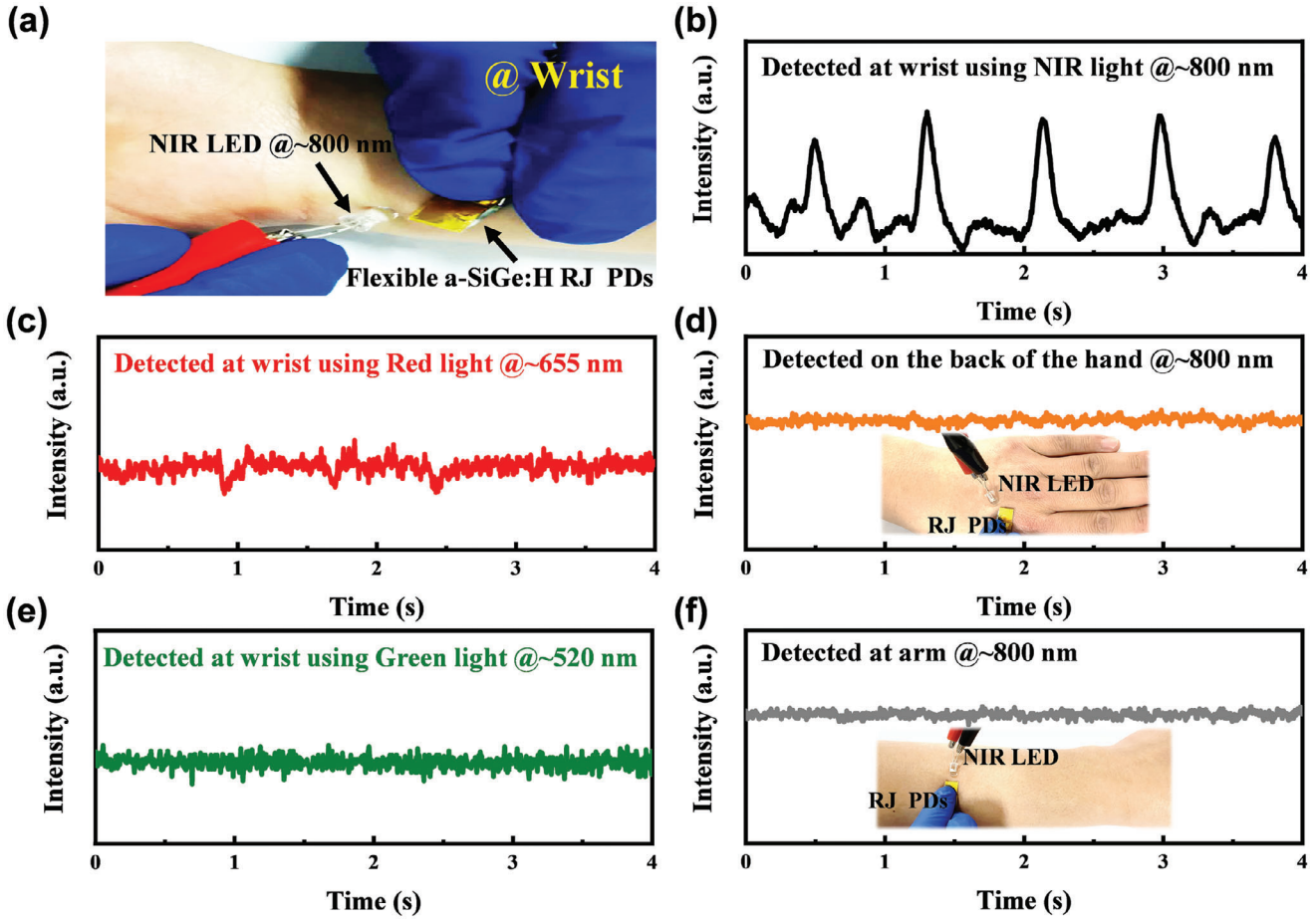


Figure 21. a) Photo of detecting pulse at the human wrist, b) detected pulse PPG signal at the wrist using NIR light as the source and detected curves at the wrist using c) red and e) green light as sources, as well as detected curves d) at vein on the back of the hand, and f) at arm without any artery, respectively.[126] Copyright 2022 Wiley-VCH GmbH, Weinheim.

volume change directly caused by heartbeat, providing thus a complementary for more accurate and efficient diagnostics and real-time health monitoring.

5. Conclusion and Perspectives

Different from the well-established wisdom in industrial-mature planar junction thin film devices, such RJ structured a-Si:H thin film optoelectronics have a long way to go before they can be realized commercially. Herein, we have reviewed some recent progress of flexible RJ optoelectronics, which can be fabricated in a PECVD system via a low-temperature VLS process by using LMP metals (such as Sn, In, Bi and their alloy) as catalysts, and directly upon the low-cost flexible substrate, such as Al foil, which has been proven to be compatible with the Roll-to-Roll thin film technology. The out-of-plane RJ section supported by the standing SiNWs framework, which is grown on the surface of the flexible substrate, can be well separated and protected from the stress-rich and unstable bottom regions. Such 3D RJ structure design provides a new dimension to develop flexible, lightweight, robust, and mechanically stable optoelectronics, which can boost the development of wearable and portable real-time personalized health devices or other bio-applications.

Of course, to establish as a mature and reliable flexible thin film solar cell technology, there are still important issues to be further improved and verified for RJ-structured devices, such as controlling uniform distribution and geometry of large-area SiNWs and depositing conformal amorphous thin films upon randomly oriented SiNWs. Addressing these issues requires a comprehensive and profound understanding of key growth mechanisms and dynamics of LMP-metal-catalyzed SiNW, as well as fabrication parameters of depositing amorphous thin film. Also, unique geometric tilting and arrangement of RJ can result in a non-uniform light absorption distribution along the length of the RJ, thus leading to a photocurrent generation gradient that imposes a limit for achieving a high voltage output. Besides, the light scattering realized among the SiNW framework dominates light harvesting in the RJ unit, which indicates that the incident photons can travel through the RJ units in multiple passes, thus an extremely transparent conductive oxide layer is needed to reduce parasitic absorption as much as possible even at the cost of conductivity.

Nevertheless, a brighter future is ahead for the RJ structured optoelectronics that are fabricated directly upon the VLS-grown

© 2024 Wiley-VCH GmbH

21951071, 2024, 9, Downloaded from https://advanced.onlinelibrary.wiley.com/doi/10.1002/adom.202302121 by Nanjing University, Wiley Online Library on [04/11/2026]. See the Terms and Conditions (https://onlinelibrary.wiley.com/terms-and-conditions) on Wiley Online Library for rules of use; OA articles are governed by the applicable Creative Commons License

SiNWs, especially for lightweight wearable, portable flexible applications. Besides, it is interesting and attractive to make full use of the advantages of a single RJ unit, for cellular stimulation or a nanometer-sized color recognizer that can act as an artificial retinal nerve, such as *p-i-n-i-p*, and for use in other biological applications.

Acknowledgements

The authors acknowledge the financial supports received from the National Key Research Program of China under granted No. 92164201, the National Natural Science Foundation of China for Distinguished Young Scholars under granted No. 62325403, the Innovation technology platform project jointly built by Yangzhou City and Yangzhou University (No. YZ2020268).

Conflict of Interest

The authors declare no conflict of interest.

Keywords

bio-applications, flexible optoelectronics, low-temperature VLS process, radial junction

Received: September 1, 2023
Revised: December 20, 2023
Published online: January 15, 2024

[1] E. Singh, P. Singh, K. S Kim, G. Y. Yeom, H. S. Nalwa, *ACS Appl. Mater. Interfaces* **2019**, *11*, 11061.
[2] T.-H. Kim, C.-S. Lee, S. Kim, J. Hur, S. Lee, K. W. Shin, Y.-Z. Yoon, M. K. Choi, J. Yang, D.-H. Kim, T. Hyeon, S. Park, S. Hwang, *ACS Nano* **2017**, *11*, 5992.
[3] Y. Pei, Z. Li, B. Li, Y. Zhao, H. He, L. Yan, X. Li, J. Wang, Z. Zhao, Y. Sun, Z. Zhou, J. Zhao, R. Guo, J. Chen, X. Yan, *Adv. Funct. Mater.* **2022**, *32*, 2203454.
[4] Z. Song, S. Zhou, Y. Qin, X. Xia, Y. Sun, G. Han, T. Shu, L. Hu, Q. Zhang, *Biosensors* **2023**, *13*, 630.
[5] T. Pan, S. Liu, L. Zhang, W. Xie, *iScience* **2022**, *25*, 103782.
[6] J. Yu, X. Hou, J. He, M. Cui, C. Wang, W. Geng, J. Mu, B. Han, X. Chou, *Nano Energy* **2020**, *69*, 104437.
[7] A K. Bansal, S. Hou, O. Kulyk, E M. Bowman, I D. W. Samuel, *Adv. Mater.* **2015**, *27*, 7638.
[8] B. Yan, Y. Zhuang, Y. Jiang, W. Xu, Y. Chen, J. Tu, X. Wang, Q. Wu, *Appl. Surf. Sci.* **2018**, *458*, 382.
[9] C. Dhote, A. Singh, S. Kumar, *IEEE Sens. J.* **2022**, *22*, 18228.
[10] N. El-Atab, W. Babatain, R. Bahabry, R. Alshanbari, R. Shamsuddin, M. M. Hussain, *ACS Appl. Mater. Interfaces* **2020**, *12*, 2269.
[11] J. He, P. Gao, J. Sheng, X. Yang, S. Zhou, Z. Ying, J. Ye, *Mater. Res. Express* **2015**, *2*, 065902.
[12] S. Saha, M. M. Hilali, E. U. Onyegam, S. Sonde, R A. Rao, L. Mathew, A. Upadhyaya, S K. Banerjee, *ECS J. Solid State Sci. Technol.* **2014**, *3*, Q142.
[13] J. He, P. Gao, M. Liao, X. Yang, Z. Ying, S. Zhou, J. Ye, Y. Cui, *ACS Nano* **2015**, *9*, 6522.
[14] M. Xue, K. N. Nazif, Z. Lyu, J. Jiang, C.-Y. Lu, N. Lee, K. Zang, Y. Chen, T. Zheng, T I. Kamins, M L. Brongersma, K. C. Saraswat, J. S. Harris, *Nano Energy* **2020**, *70*, 104466.
[15] K.-T. Park, H.-J. Kim, M.-J. Park, J.-H. Jeong, J. Lee, D.-G. Choi, J.-H. Lee, J.-H. Choi, *Sci. Rep.* **2015**, *5*, 12093.
[16] S.-S. Yoon, D.-Y. Khang, *ACS Appl. Mater. Interfaces* **2019**, *11*, 3290.
[17] S. Lee, J. Hong, J. H. Koo, S. Lee, K. Lee, S. Im, T. Lee, *IEEE T. Electron. Dev.* **2011**, *58*, 3329.
[18] B.-C. Zhang, Y.-H. Shi, J. Mao, S.-Y. Huang, Z.-B. Shao, C.-J. Zheng, J.-S. Jie, X.-H. Zhang, *Adv. Mater.* **2021**, *33*, 2008171.
[19] J.-Y. Chen, C. Con, M.-H. Yu, B. Cui, K. W. Sun, *ACS Appl. Mater. Interfaces* **2013**, *5*, 7552.
[20] K. W. Chang, K. W. Sun, *Org. Electron.* **2018**, *55*, 82.
[21] J. Song, G. Tang, J. Cao, H. Liu, Z. Zhao, S. Griggs, A. Yang, N. Wang, H. Cheng, C.-K. Liu, I. Mcculloch, F. Yan, *Adv. Mater.* **2023**, *35*, 2207763.
[22] Z. Liu, B. Wen, L. Cao, S. Zhang, Y. Lei, G. Zhao, L. Chen, J. Wang, Y. Shi, J. Xu, X. Pan, L. Yu, *Adv. Healthcare Mater.* **2020**, *9*, 1901342.
[23] H. C. Ko, M P. Stoykovich, J. Song, V. Malyarchuk, W. M. Choi, C.-J. Yu, J. B. Geddes Iii, J. Xiao, S. Wang, Y. Huang, J. A. Rogers, *Nature* **2008**, *454*, 748.
[24] G. Simone, D. Di Carlo Rasi, X. De Vries, G. H. L. Heintges, S. C. J. Meskers, R. A. J. Janssen, G. H. Gelinck, *Adv. Mater.* **2018**, *30*, 1804678.
[25] Z. Huang, L. Li, T. Wu, T. Xue, W. Sun, Q. Pan, H. Wang, H. Xie, J. Chi, T. Han, X. Hu, M. Su, Y. Chen, Y. Song, *Nat. Commun.* **2023**, *14*, 1204.
[26] K. Miettunen, J. Vapaavuori, A. Poskela, A. Tiihonen, P D. Lund, *WIREs Energy Environ.* **2018**, *7*, 302.
[27] K. Liu, S. Chen, D. Ba, D. Wang, Y. Ba, G. Du, H. Liu, *J. Comput. Theor. Nanosci.* **2015**, *12*, 2931.
[28] K. Ahn, S.-Y. Kim, S. Kim, D.-H. Son, S.-H. Kim, S. Kim, J. Kim, S.-J. Sung, D.-H. Kim, J.-K. Kang, *J. Mater. Chem. A* **2019**, *7*, 24891.
[29] P C. Y. Chow, T. Someya, *Adv. Mater.* **2020**, *32*, 1902045.
[30] H. Ren, J.-D. Chen, Y.-Q. Li, J.-X. Tang, *Adv. Sci.* **2020**, *8*, 2002418.
[31] D. P. Dubal, N. R. Chodankar, D.-H. Kim, P. Gomez-Romero, *Chem. Soc. Rev.* **2018**, *47*, 2065.
[32] Y. Khan, D. Han, J. Ting, M. Ahmed, R. Nagisetty, A. C. Arias, *IEEE Access* **2019**, *7*, 128114.
[33] X. Xu, Y. Zhao, Y. Liu, *Small* **2023**, *19*, 2206309.
[34] R. D. Pensack, K. M. Banyas, L. W. Barbour, M. Hegadorn, J. B. Asbury, *Phys. Chem. Chem. Phys.* **2009**, *11*, 2575.
[35] P. Mittal, S. Yadav, S. Negi, *Mater. Sci. Semicond. Process.* **2021**, *133*, 105975.
[36] Y.-F. Chang, Z.-Y. Lu, L.-J. An, J.-P. Zhang, *J. Phys. Chem. C* **2011**, *116*, 1195.
[37] D. Yeboah, J. Singh, *J. Mater. Sci. Mater. Electron.* **2018**, *29*, 13354.
[38] H. Li, N. Tessler, J.-L. Brédas, *Adv. Funct. Mater.* **2018**, *28*, 1803096.
[39] M. Ellis, H. Yang, S. Giannini, O. G. Ziogos, J. Blumberger, *Adv. Mater.* **2021**, *33*, 2104852.
[40] M. Koopmans, M. A. T. Leiviskä, J. Liu, J. Dong, L. Qiu, J. C. Hummelen, G. Portale, M. C. Heiber, L. J. A. Koster, *ACS Appl. Mater. Interfaces* **2020**, *12*, 56222.
[41] P. Docampo, J. M. Ball, M. Darwich, G. E. Eperon, H. J. Snaith, *Nat. Commun.* **2013**, *4*, 2761.
[42] G. Tong, H. Li, D. Li, Z. Zhu, E. Xu, G. Li, L. Yu, J. Xu, Y. Jiang, *Small* **2018**, *14*, 1702523.
[43] K.-G. Lim, T.-H. Han, T.-W. Lee, *Energy Environ. Sci.* **2021**, *14*, 2009.
[44] H. Chen, H. Wang, J. Wu, F. Wang, T. Zhang, Y. Wang, D. Liu, S. Li, R. V. Penty, I. H. White, *Nano Res.* **2020**, *13*, 1997.
[45] Y. Wang, D. Li, L. Chao, T. Niu, Y. Chen, W. Huang, *Appl. Mater. Today* **2022**, *28*, 101509.
[46] D. Ding, H. Li, H. Yao, L. Liu, B. Tian, C. Su, Y. Wang, Y. Shi, *J. Mater. Chem. C* **2019**, *7*, 9496.
[47] L.-B. Luo, G.-A. Wu, Y. Gao, L. Liang, C. Xie, Z.-X. Zhang, X.-W. Tong, T. Wang, F.-X. Liang, *Adv. Optical Mater.* **2019**, *7*, 1900272.
[48] C. Li, J.-X. Li, C.-Y. Li, J. Wang, X.-W. Tong, Z.-X. Zhang, Z.-P. Yin, D. Wu, L.-B. Luo, *Adv. Optical Mater.* **2021**, *9*, 2100371.

© 2024 Wiley-VCH GmbH

21951071, 2024, 9, Downloaded from https://advanced.onlinelibrary.wiley.com/doi/10.1002/adom.202302121 by Nanjing University, Wiley Online Library on [04/11/2026]. See the Terms and Conditions (https://onlinelibrary.wiley.com/terms-and-conditions) on Wiley Online Library for rules of use; OA articles are governed by the applicable Creative Commons License

[49] X. Mathew, J. P Enriquez, A. Romeo, A. N. Tiwari, *Sol. Energy* **2004**, *77*, 831.
[50] A. Salavei, D. Menossi, F. Piccinelli, A. Kumar, G. Mariotto, M. Barbato, M. Meneghini, G. Meneghesso, S. Di Mare, E. Artegiani, A. Romeo, *Sol. Energy* **2016**, *139*, 13.
[51] X. Mathew, *Sol. Energy Mater. Sol. Cells* **2003**, *76*, 293.
[52] L. Kranz, C. Gretener, J. Perrenoud, R. Schmitt, F. Pianezzi, F. La Mattina, P. Blösch, E. Cheah, A. Chirila, C M. Fella, H. Hagendorfer, T. Jäger, S. Nishiwaki, A R. Uhl, S. Buecheler, A N. Tiwari, *Nat. Commun.* **2013**, *4*, 2306.
[53] A. N. Tiwari, A. Romeo, D. Baetzner, H. Zogg, *Prog. Photovolt: Res. Appl.* **2001**, *9*, 211.
[54] K. Kim, J. Kim, M. G. Gang, S.-H. Kim, S. Song, Y. Cho, D. Shin, Y.-J. Eo, I. Jeong, S. K. Ahn, A. Cho, J. Kim, S. Yoon, P.-P. Choi, W. Jo, J. H. Kim, J. Gwak, J. H. Yun, *Sol. Energy Mater. Sol. Cells* **2019**, *195*, 280.
[55] P. Reinhard, A. Chirila, P. Blosch, F. Pianezzi, S. Nishiwaki, S. Buecheler, A N. Tiwari, *IEEE J. Photovolt.* **2013**, *3*, 572.
[56] S. Shi, L. Yao, P. Ma, Y. Jiao, X. Zheng, D. Ning, M. Chen, F. Sui, H. Liu, C. Yang, W. Li, *Mater. Today Energy* **2021**, *20*, 100640.
[57] D J. Hwang, S. Kuk, Z. Wang, S. Fu, T. Zhang, G. Kim, W. M. Kim, J.-H. Jeong, *Appl. Phys. A* **2016**, *123*, 55.
[58] J.-K. Sim, S. Kang, R. Nandi, J.-Y. Jo, K.-U. Jeong, C.-R. Lee, *Sol. Energy* **2018**, *162*, 357.
[59] J. Ramanujam, D M. Bishop, T K. Todorov, O. Gunawan, J. Rath, R. Nekovei, E. Artegiani, A. Romeo, *Prog. Mater. Sci.* **2020**, *110*, 100619.
[60] Y.-C. Wang, T.-T. Wu, Y.-L. Chueh, *Mater. Chem. Phys.* **2019**, *234*, 329.
[61] X. Dai, S. Zhang, Z. Wang, G. Adamo, H. Liu, Y. Huang, C. Couteau, C. Soci, *Nano Lett.* **2014**, *14*, 2688.
[62] A. Cretì, P. Prete, N. Lovergine, M. Lomascolo, *ACS Appl. Nano Mater* **2022**, *5*, 18149.
[63] C. Xie, X.-T. Lu, M.-R. Ma, X.-W. Tong, Z.-X. Zhang, L. Wang, C.-Y. Wu, W.-H. Yang, L.-B. Luo, *Adv. Optical Mater.* **2019**, *7*, 1901257.
[64] C. Yang, J. Qu, Z. Wu, *Sol. Energy* **2021**, *214*, 542.
[65] J. Long, X. Li, Q. Sun, P. Dai, Y. Zhang, J. Xuan, F. Chen, M. Song, S. Honda, S. Uchida, S. Lu, *Sol. RRL* **2021**, *5*, 2100066.
[66] D. J. You, S. H. Kim, H. Lee, J.-W. Chung, S.-T. Hwang, Y. H. Heo, S. Lee, H.-M. Lee, *Prog. Photovolt: Res. Appl.* **2015**, *23*, 973.
[67] A. V. Shah, H. Schade, M. Vanecek, J. Meier, E. Vallat-Sauvain, N. Wyrsch, U. Kroll, C. Droz, J. Bailat, *Prog. Photovolt: Res. Appl.* **2004**, *12*, 113.
[68] M. A. Green, *Prog. Photovolt: Res. Appl.* **2001**, *9*, 123.
[69] A. Terakawa, *Sol. Energy Mater. Sol. Cells* **2013**, *119*, 204.
[70] R. Yang, C.-H. Lee, B. Cui, A. Sazonov, *Mat. Sci. Eng. B* **2018**, *229*, 1.
[71] Q. Lin, L. Lu, M. M. Tavakoli, C. Zhang, G. C. Lui, Z. Chen, X. Chen, L. Tang, D. Zhang, Y. Lin, P. Chang, D. Li, Z. Fan, *Nano Energy* **2016**, *22*, 539.
[72] C. Hengst, S. Menzel, G. Rane, V. Smirnov, K. Wilken, B. Leszczynska, D. Fischer, N. Prager, *Materials* **2017**, *10*, 245.
[73] Z. Wang, L. Peng, Z. Lin, J. Ni, P. Yi, X. Lai, X. He, Z. Lei, *Sci. Rep.* **2017**, *7*, 13155.
[74] S. Cao, D. Yu, Y. Lin, C. Zhang, L. Lu, M. Yin, X. Zhu, X. Chen, D. Li, *ACS Appl. Mater. Interfaces* **2020**, *12*, 26184.
[75] C. Zhang, Y. Song, M. Wang, M. Yin, X. Zhu, L. Tian, H. Wang, X. Chen, Z. Fan, L. Lu, D. Li, *Adv. Funct. Mater.* **2017**, *27*, 1604720.
[76] S. Misra, L. Yu, M. Foldyna, P. Roca I Cabarrocas, *Sol. Energy Mater. Sol. Cells* **2013**, *118*, 90.
[77] X. Sun, T. Zhang, J. Wang, F. Yang, L. Xu, J. Xu, Y. Shi, K. Chen, P. Roca I Cabarrocas, L. Yu, *Nano Energy* **2018**, *53*, 83.
[78] S. Zhang, T. Zhang, Z. Liu, J. Wang, L. Yu, J. Xu, K. Chen, P. Roca I Cabarrocas, *Nano Energy* **2021**, *86*, 106121.
[79] S. Zhang, T. Zhang, L. Cao, Z. Liu, J. Wang, J. Xu, K. Chen, L. Yu, *Opt. Express* **2019**, *27*, 37248.
[80] W. J. Dong, S. Kim, J. Y. Park, H. K. Yu, J.-L. Lee, *ACS Appl. Mater. Interfaces* **2019**, *11*, 30477.
[81] W. J. Dong, C. J. Yoo, H. W. Cho, K.-B. Kim, M. Kim, J.-L. Lee, *Small* **2015**, *11*, 1947.
[82] N. I. Goktas, P. Wilson, A. Ghukasyan, D. Wagner, S. Mcnamee, R. R. Lapierre, *Appl. Phys. Rev.* **2018**, *5*, 041305.
[83] G. Cao, X. Li, Y. Zhan, S. Wu, A. Shang, C. Zhang, Z. Yang, X. Zhai, *Opt. Express* **2014**, *22*, A1761.
[84] E. C. Garnett, M. L. Brongersma, Y. Cui, M. D. Mcgehee, *Annu. Rev. Mater. Res.* **2011**, *41*, 269.
[85] E. C. Garnett, P. Yang, *J. Am. Chem. Soc.* **2008**, *130*, 9224.
[86] G. Jia, A. Gawlik, J. Bergmann, B. Eisenhawer, S. Schonherr, G. Andra, F. Falk, *IEEE J. Photovolt.* **2014**, *4*, 28.
[87] L. Tsakalakos, J. Balch, J. Fronheiser, B. A. Korevaar, O. Sulima, J. Rand, *Appl. Phys. Lett.* **2007**, *91*, 233117.
[88] L. Cao, J. S. White, J.-S. Park, J. A. Schuller, B. M. Clemens, M. L. Brongersma, *Nat. Mater.* **2009**, *8*, 643.
[89] M. M. Adachi, M. P. Anantram, K. S. Karim, *Sci. Rep.* **2013**, *3*, 1546.
[90] R.-E. Nowak, M. Vehse, O. Sergeev, K. Von Maydell, C. Agert, *Sol. Energy Mater. Sol. Cells* **2014**, *125*, 305.
[91] Z. Li, X. Liang, G. Li, H. Liu, H. Zhang, J. Guo, J. Chen, K. Shen, X. San, W. Yu, R E. I. Schropp, Y. Mai, *Nat. Commun.* **2019**, *10*, 125.
[92] Y. Kuang, M. C. Van Lare, L. W. Veldhuizen, A. Polman, J. K. Rath, R. E. I. Schropp, *J. Appl. Phys.* **2015**, *118*, 185307.
[93] J. R. Sharma, S. Mitra, H. Ghosh, G. Das, S. Bose, S. Mandal, S. Mukhopadhyay, H. Saha, A. K. Barua, *Physica B Condens. Matter* **2018**, *530*, 147.
[94] A. P. Amalathas, M. M. Alkaisi, *Int. J. Nanotechnol.* **2017**, *14*, 3.
[95] D. Shi, Y. Zeng, W. Shen, *Sci. Rep.* **2015**, *5*, 16504.
[96] A. S. M. Mohsin, S. Mondal, M. Mobashera, A. Malik, M. Islam, M. Rubaiat, *Heliyon* **2023**, *9*, 16749.
[97] J. Buencuerpo, J. M. Llorens, M. L. Dotor, J. M. Ripalda, *Opt. Express* **2015**, *23*, A322.
[98] Z. Zhang, B. Qiu, B. Shao, X. Wu, R. Zhang, *Jpn. J. Appl. Phys.* **2015**, *54*, 062301.
[99] Q. G. Du, C. H. Kam, H. V. Demir, H. Y. Yu, X. W. Sun, *Opt. Lett.* **2011**, *36*, 1713.
[100] W. Q. Xie, W. F. Liu, J. I. Oh, W. Z. Shen, *Appl. Phys. Lett.* **2011**, *99*, 033107.
[101] M. Gharghi, E. Fathi, B. Kante, S. Sivoththaman, X. Zhang, *Nano Lett.* **2012**, *12*, 6278.
[102] K. Li, X. Wang, P. Lu, J. Ding, N. Yuan, *Sol. Energy Mater. Sol. Cells* **2014**, *128*, 11.
[103] B. Pal, K. J. Sarkar, S. Das, P. Banerji, *J. Alloys Compd.* **2021**, *885*, 160943.
[104] B. Pal, K. J. Sarkar, P. Banerji, *Sol. Energy Mater. Sol. Cells* **2020**, *204*, 110217.
[105] C. Cheng, T.-L. Wang, L. Feng, W. Li, K. M. Ho, M. M. T. Loy, K. K. Fung, N. Wang, *Nanotechnology* **2010**, *21*, 475703.
[106] M. Pathirane, B. Iheanacho, A. Tamang, C.-H. Lee, R. Lujan, D. Knipp, W. S. Wong, *Appl. Phys. Lett.* **2015**, *107*, 143903.
[107] M. K. Pathirane, W. S. Wong, *Small* **2016**, *12*, 2554.
[108] H. Zeng, X. Yu, H. A. Fonseka, J. A. Gott, M. Tang, Y. Zhang, G. Boras, J. Xu, A. M. Sanchez, H. Liu, *Nano Lett.* **2018**, *18*, 6397.
[109] D. Spirkoska, J. Arbiol, A. Gustafsson, S. Conesa-Boj, F. Glas, I. Zardo, M. Heigoldt, M. H. Gass, A. L. Bleloch, S. Estrade, M. Kaniber, J. Rossler, F. Peiro, J. R. Morante, G. Abstreiter, L. Samuelson, A. Fontcuberta I Morral, *Phys. Rev. B* **2009**, *80*, 245325.
[110] E. Uccelli, J. Arbiol, C. Magen, P. Krogstrup, E. Russo-Averchi, M. Heiss, G. Mugny, F. Morier-Genoud, J. Nygård, J. R. Morante, A. Fontcuberta I Morral, *Nano Lett.* **2011**, *11*, 3827.
[111] F.-X. Liang, J.-Z. Wang, Z.-P. Li, L.-B. Luo, *Adv. Optical Mater.* **2017**, *5*, 1700081.
[112] Y. Zhu, V. Raj, Z. Li, H. H. Tan, C. Jagadish, L. Fu, *Adv. Mater.* **2021**, *33*, 2105729.

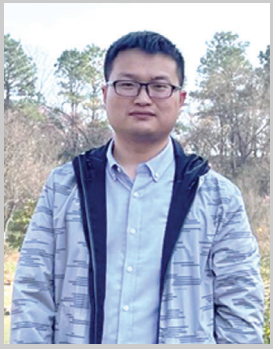
© 2024 Wiley-VCH GmbH

21951071, 2024, 9, Downloaded from https://advanced.onlinelibrary.wiley.com/doi/10.1002/adom.202302121 by Nanjing University, Wiley Online Library on [04/11/2026]. See the Terms and Conditions (https://onlinelibrary.wiley.com/terms-and-conditions) on Wiley Online Library for rules of use; OA articles are governed by the applicable Creative Commons License

[113] P. Krogstrup, H. I. Jørgensen, M. Heiss, O. Demichel, J. V. Holm, M. Aagesen, J. Nygard, A. Fontcuberta I Morral, *Nat. Photonics* **2013**, *7*, 306.
[114] K. Minehisa, R. Murakami, H. Hashimoto, K. Nakama, K. Sakaguchi, R. Tsutsumi, T. Tanigawa, M. Yukimune, K. Nagashima, T. Yanagida, S. Sato, S. Hiura, A. Murayama, F. Ishikawa, *Nanoscale Adv* **2023**, *5*, 1651.
[115] A. Mukherjee, D. Ren, P.-E. Vullum, J. Huh, B.-O. Fimland, H. Weman, *ACS Photonics* **2021**, *8*, 2355.
[116] K. Zhang, X. Li, W. Dai, F. Toor, J. P. Prineas, *Nano Lett.* **2019**, *19*, 4272.
[117] X. Li, K. Zhang, J. Treu, L. Stampfer, G. Koblmueller, F. Toor, J. P. Prineas, *Nano Lett.* **2019**, *19*, 990.
[118] C. Affentauschegg, H. H. Wieder, *Semicond. Sci. Technol.* **2001**, *16*, 708.
[119] H. Zhang, X. Dai, N. Guan, A. Messanvi, V. Neplokh, V. Piazza, M. Vallo, C. Bougerol, F. H. Julien, A. Babichev, N. Cavassilas, M. Bescond, F. Michelini, M. Foldyna, E. Gautier, C. Durand, J. Eymery, M. Tchernycheva, *ACS Appl. Mater. Interfaces* **2016**, *8*, 26198.
[120] V. Khayrudinov, M. Remennyi, V. Raj, P. Alekseev, B. Matveev, H. Lipsanen, T. Haggren, *ACS Nano* **2020**, *14*, 7484.
[121] M. K. Sahoo, P. Kale, *J. Materiomics* **2019**, *5*, 34.
[122] M. Konagai, *Jpn. J. Appl. Phys.* **2011**, *50*, 030001.
[123] M. Stuckelberger, R. Biron, N. Wyrsch, F.-J. Haug, C. Ballif, *Renew. Sust. Energ. Rev.* **2017**, *76*, 1497.
[124] S. Misra, L. Yu, W. Chen, M. Foldyna, P. R. I. Cabarrocas, *J. Phys. D: Appl. Phys.* **2014**, *47*, 393001.
[125] T. Zhang, J. Wang, L. Yu, J. Xu, P. Roca I Cabarrocas, *Nanotechnology* **2019**, *30*, 302001.
[126] S. Zhang, T. Zhang, Z. Liu, J. Wang, J. Xu, K. Chen, L. Yu, *Adv. Funct. Mater.* **2022**, *32*, 2107040.
[127] R. S. Wagner, W. C. Ellis, *Appl. Phys. Lett.* **1964**, *4*, 89.
[128] V. Schmidt, J. V. Wittemann, U. Gösele, *Chem. Rev.* **2010**, *110*, 361.
[129] M C. Putnam, M A. Filler, B M. Kayes, M D. Kelzenberg, Y. Guan, N S. Lewis, J M. Eiler, H A. Atwater, *Nano Lett.* **2008**, *8*, 3109.
[130] S. M. Sze, *Physics of Semiconductor Devices*, Vol. *1*, Wiley, New York **1981**.
[131] Y. Ichikawa, T. Yoshida, T. Hama, H. Sakai, K. Harashima, *Sol. Energy Mater. Sol. Cells* **2001**, *66*, 107.
[132] H. Nishiwaki, K. Uchihashi, K. Takaoka, M. Nakagawa, H. Inoue, A. Takeoka, S. Tsuda, M. Ohnishi, *Sol. Energy Mater. Sol. Cells* **1995**, *37*, 295.
[133] L. Yu, B. O'donnell, P.-J. Alet, S. Conesa-Boj, F. Peiró, J. Arbiol, P. R. I. Cabarrocas, *Nanotechnology* **2009**, *20*, 225604.
[134] L. Yu, F. Fortuna, B. O'donnell, T. Jeon, M. Foldyna, G. Picardi, P. Roca I Cabarrocas, *Nano Lett.* **2012**, *12*, 4153.
[135] L. Yu, B. O'donnell, M. Foldyna, P. Roca I Cabarrocas, *Nanotechnology* **2012**, *23*, 194011.
[136] I. Zardo, L. Yu, S. Conesa-Boj, S. Estradé, P. J. Alet, J. Rössler, M. Frimmer, P. Roca I Cabarrocas, F. Peiró, J. Arbiol, J. R. Morante, A. Fontcuberta I Morral, *Nanotechnology* **2009**, *20*, 155602.
[137] P.-J. Alet, L. Yu, G. Patriarche, S. Palacin, P. Roca I Cabarrocas, *J. Mater. Chem.* **2008**, *18*, 5187.
[138] L. Yu, F. Fortuna, B. O'donnell, G. Patriache, P. Roca I Cabarrocas, *Appl. Phys. Lett.* **2011**, *98*, 123113.
[139] V. A. Nebol'sin, A. A. Shchetinin, *Inorg. Mater.* **2003**, *39*, 899.
[140] V. A. Nebol'sin, A. A. Shchetinin, A. N. Korneeva, A. I. Dunaev, A. A. Dolgachev, T. I. Sushko, A. F. Tatarenkov, *Inorg. Mater.* **2006**, *42*, 339.
[141] V. Schmidt, J. V. Wittemann, S. Senz, U. Gösele, *Adv. Mater.* **2009**, *21*, 2681.
[142] M. I. Den Hertog, J.-L. Rouviere, F. Dhalluin, P. J. Desré, P. Gentile, P. Ferret, F. Oehler, T. Baron, *Nano Lett.* **2008**, *8*, 1544.
[143] C.-Y. Wen, J. Tersoff, M. C. Reuter, E. A. Stach, F. M. Ross, *Phys. Rev. Lett.* **2010**, *105*, 195502.
[144] S. Misra, L. Yu, M. Foldyna, P. Roca I Cabarrocas, *IEEE J. Photovolt.* **2015**, *5*, 40.
[145] H. Tarui, T. Matsuyama, S. Okamoto, H. Dohjoh, Y. Hishikawa, N. Nakamura, S. Tsuda, S. Nakano, M. Ohnishi, Y. Kuwano, *Jpn. J. Appl. Phys.* **1989**, *28*, 2436.
[146] M. Isomura, T. Takahama, S. T. Shinya Tsuda, S. N. Shoichi Nakano, *Jpn. J. Appl. Phys.* **1993**, *32*, 1902.
[147] E. Garnett, P. Yang, *Nano Lett.* **2010**, *10*, 1082.
[148] J. Lu, S. Qian, Z. Yu, S. Misra, L. Yu, J. Xu, Y. Shi, P. Roca I Cabarrocas, K. Chen, *Opt. Express* **2015**, *23*, A1288.
[149] H. Zhang, Y. Lei, Q. Zhu, T. Qing, T. Zhang, W. Tian, M. Lange, M. Jiang, C. Han, J. Li, D. Koelle, R. Kleiner, W.-W. Xu, Y. Wang, L. Yu, H. Wang, P. Wu, *ACS Nano* **2019**, *13*, 10359.
[150] J. Kim, M. Lee, H. J. Shim, R. Ghaffari, H. R. Cho, D. Son, Y. H. Jung, M. Soh, C. Choi, S. Jung, K. Chu, D. Jeon, S.-T. Lee, J. H. Kim, S. H. Choi, T. Hyeon, D.-H. Kim, *Nat. Commun.* **2014**, *5*, 5747.
[151] C. Chen, K. Li, F. Li, B. Wu, P. Jiang, H. Wu, S. Lu, G. Tu, Z. Liu, J. Tang, *ACS Photonics* **2020**, *7*, 352.
[152] F. Yang, J. Wang, J. Lu, Z. Yu, L. Yu, J. Xu, Y. Shi, K. Chen, P. Roca I Cabarrocas, *Adv. Optical Mater.* **2017**, *5*, 1700390.
[153] T. Zhang, L. Cao, S. Zhang, Z. Liu, J. Wang, Y. Shi, J. Xu, K. Chen, L. Yu, *Nano Futures* **2020**, *4*, 035007.
[154] H. Cai, D. Zhang, Y. Xue, K. Tao, *Sol. Energy Mater. Sol. Cells* **2009**, *93*, 1959.
[155] Y. Kishi, H. Inoue, K. Murata, H. Tanaka, S. Kouzuma, M. Morizane, Y. Fukuda, H. Nishiwaki, K. Nakano, A. Takeoka, M. Ohnishi, Y. Kuwano, *Sol. Energy Mater.* **1991**, *23*, 312.
[156] X. Zhang, C. Zhang, D. Li, S. Cao, M. Yin, P. Wang, G. Ding, L. Yang, J. Cheng, L. Lu, *Nanoscale Res. Lett.* **2019**, *14*, 324.
[157] O. Keles, M. Dundar, *J. Mater. Process. Technol.* **2007**, *186*, 125.
[158] H. Zhang, X.-S. Zhang, X. Cheng, Y. Liu, M. Han, X. Xue, S. Wang, F. Yang, S. A. Smitha, H. Zhang, Z. Xu, *Nano Energy* **2015**, *12*, 296.
[159] G.-T. Hwang, M. Byun, C. K. Jeong, K. J. Lee, *Adv. Healthcare Mater.* **2015**, *4*, 646.
[160] B. Shi, Z. Li, Y. Fan, *Adv. Mater.* **2018**, *30*, 1801511.
[161] Q. Zheng, B. Shi, F. Fan, X. Wang, L. Yan, W. Yuan, S. Wang, H. Liu, Z. Li, Z. L. Wang, *Adv. Mater.* **2014**, *26*, 5851.
[162] L. Bereuter, S. Williner, F. Pianezzi, B. Bissig, S. Buecheler, J. Burger, R. Vogel, A. Zurbuchen, A. Haeberlin, *Ann. Biomed. Eng.* **2017**, *45*, 1172.
[163] G.-T. Hwang, H. Park, J.-H. Lee, S. Oh, K.-I. Park, M. Byun, H. Park, G. Ahn, C. K. Jeong, K. No, H. Kwon, S.-G. Lee, B. Joung, K. J. Lee, *Adv. Mater.* **2014**, *26*, 4880.
[164] A. Rogalski, *Infrared Phys. Techn.* **2002**, *43*, 187.
[165] L. A. Bortolotto, J. Blacher, T. Kondo, K. Takazawa, M. E. Safar, *Am. J. Hypertens.* **2000**, *13*, 165.
[166] J. Allen, *Physiol. Meas.* **2007**, *28*, R1.
[167] J. Y. A. Foo, C. S. Lim, P. Wang, *Physiol. Meas.* **2006**, *27*, 685.
[168] J. Li, H. Duan, K. Pu, *Adv. Mater.* **2019**, *31*, 1901607.
[169] S. Chen, A. Z. Weitemier, X. Zeng, L. He, X. Wang, Y. Tao, A J. Y. Huang, Y. Hashimotodani, M. Kano, H. Iwasaki, L. K. Parajuli, S. Okabe, D B. L Teh, A H. All, I. Tsutsui-Kimura, K F. Tanaka, X. Liu, T. J. Mchugh, *Science* **2018**, *359*, 679.
[170] S. Manna, S. Das, S P. Mondal, R. Singha, S K. Ray, *J. Phys. Chem. C* **2012**, *116*, 7126.

© 2024 Wiley-VCH GmbH

21951071, 2024, 9, Downloaded from https://advanced.onlinelibrary.wiley.com/doi/10.1002/adom.202302121 by Nanjing University, Wiley Online Library on [04/11/2026]. See the Terms and Conditions (https://onlinelibrary.wiley.com/terms-and-conditions) on Wiley Online Library for rules of use; OA articles are governed by the applicable Creative Commons License



Shaobo Zhang received his B.S. degree and M.S. degree from China University of Mining and Technology, Xuzhou, China, in 2015 and 2018, and his Ph.D. degree from Nanjing University, Nanjing, China, in 2022. He is currently a lecturer in the College of Physical Science and Technology at Yangzhou University, Yangzhou, China. His research interests include Si nanowire-based photovoltaic devices, flexible electronics, and bio-sensors.



Linwei Yu received his B.S. degree in semiconductor physics in 2001 and his Ph.D. degree in microelectronics from Nanjing University, Nanjing, China, in 2007. From 2007 to 2009, he was a Postdoctoral Researcher at LPICM, Ecole Polytechnique, France, and then joined CNRS as a Permanent Researcher (CR2) in 2009. Since 2013, he has been a Professor in the School of Electronics Science and Engineering at Nanjing University. His research interests include the growth mechanism and application of silicon nanowires for stretchable thin film electronics, 3D logic devices, sensors, and photovoltaics.

© 2024 Wiley-VCH GmbH

21951071, 2024, 9, Downloaded from https://advanced.onlinelibrary.wiley.com/doi/10.1002/adom.202302121 by Nanjing University, Wiley Online Library on [04/11/2026]. See the Terms and Conditions (https://onlinelibrary.wiley.com/terms-and-conditions) on Wiley Online Library for rules of use; OA articles are governed by the applicable Creative Commons License